LBL-17975

Lawrence Berkeley Laboratory
UNIVERSITY OF CALIFORNIA

EARTH SCIENCES DIVISION

ANALYSIS OF CROSS-HOLE SEISMIC MEASUREMENTS IN COLUMNAR-JOINTED BASALT

J.J. Rezowalli
(M.S. Thesis)

May 1984

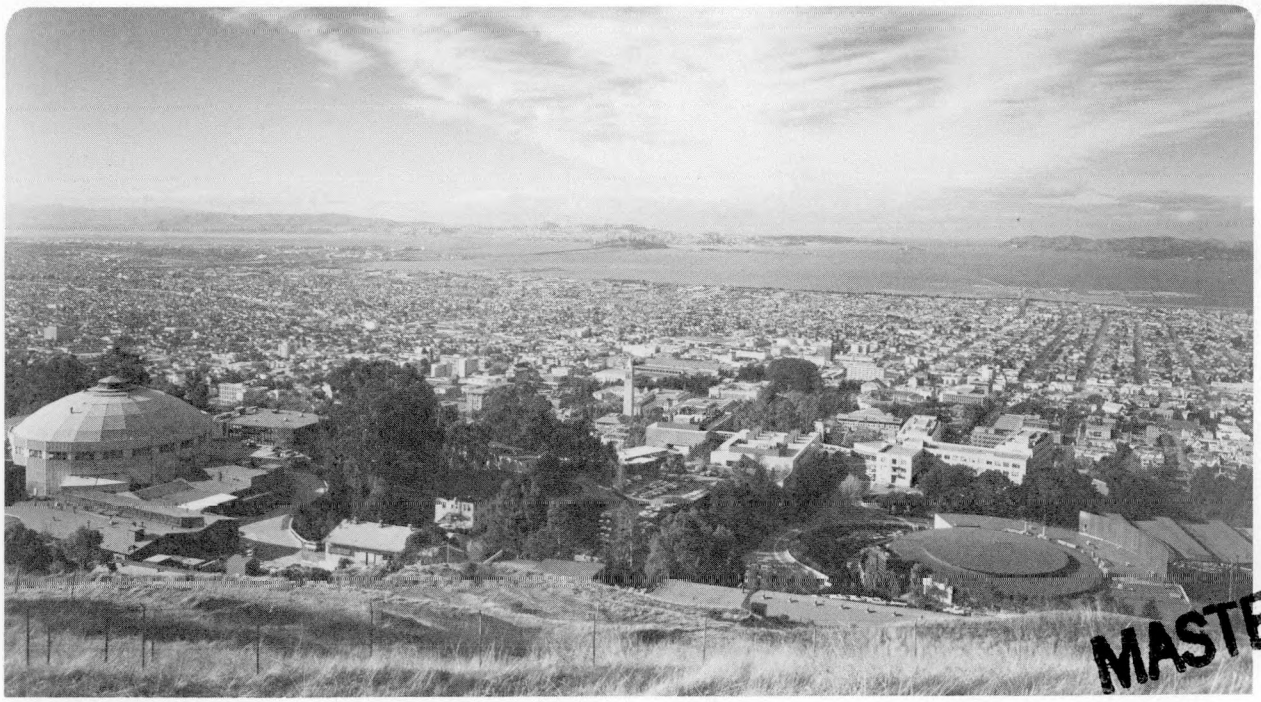

Prepared for the U.S. Department of Energy under Contract DE-AC03-76SF00098

LBL-17975

LBL--17975

DE85 007618

Analysis of Cross-Hole Seismic Measurements in Columnar-Jointed Basalt

James Jude Rezowalli

M.S. Thesis

May 1984

This work was supported in part by the Director, Office of Basic Energy Sciences, Division of Engineering, Mathematics, and Geosciences, of the U.S. Department of Energy under Contract No. DE-AC03-76SF00098.

Analysis of Cross-Hole Seismic Measurements in Columnar-Jointed Basalt

Master of Science James Rezowalli Engineering Geoscience

Signature _____
Chairman of Committee

Abstract

A series of cross-hole acoustic measurements have been performed in a columnar-jointed basaltic rock mass around an underground opening mined bu the drill-and-blast method. The purposes of the test program were: to evaluate the rock mass characteristics around the opening; to determine the zone of blast damage; and to evaluate seismic methods for anomaly detection ahead of mining in this type of rock. The cross-hole measurements were made between four 76-mm diameter horizontal boreholes diamond-drilled 12 m into a wall of the underground opening. Repetitive pulses of compressional (P) and shear (S) waves of frequencies in the range of 1 kHz-100 kHz were propagated from a transmitter sonde through the rock mass to a receiver sonde, both of which were clamped hydraulically to the borehole wall. After amplification the received P- and S-wave signals were digitized at the surface by a digital oscilloscope and stored on floppy discs.

The results indicate considerable reductions in P- and S-wave velocities at distances less than 2 m from the face. Clearly these low values are associated with blast damage. Beyond 2 m, the velocities in a vertical direction indicate almost constant values. The

velocities in the horizontal direction beyond 2 m appeared erratic, but showed a general tendency to increase as a function of distance from the face. Their maximum values remained, however, still lower in value than the corresponding velocities in the vertical direction. Near the face, the differences in velocities were considerably greater: with horizontal velocities considerably lower in value than those vertical. Results of the spectral analyses of the received signals indicated that Q-values were strongly influenced by the vertically-oriented sets of joints. Only for waves travelling in the vertical direction was the effect observed of the blast-damaged zone immediately around the opening.

The acoustic data obtained are clearly indicative of an anisotropic jointed rock mass, with a greater intensity of jointing for travel paths in the horizontal than the vertical direction. The vertical, columnar joints are probably less tightly closed than those oriented in the horizontal plane.

Acknowledgements

I would like to express my deep appreciation to Dr. Michael King of Lawrence Berkeley Laboratory for providing the opportunity and direction that made this thesis possible. I would like to thank Dr. Larry Myer for accepting, with good humor, my periodic calls from the field for advice when things were not operating as precisely as engineered, and to Dr. Ernie Majer for support and much useful information. I would also like to thank Dr. Frank Morrison and Dr. Tom McEvilly for reading this thesis, and Dave Lanigan and the crew at the Near-Surface Test Facility for their invaluable help collecting the data.

I would also like to express my thanks to my family, my grandmother Lucy Rezowalli and my aunt Marthe Bourdieu, for their moral support. Lastly, I would like to thank Margaret Wing for keeping me happy and sane through the two years I have spent working towards my degree.

Contents

1. Introduction

1.1. Introduction

This thesis contains descriptions of a series of cross-borehole seismic tests performed in a columnar jointed basalt and a subsequent laboratory investigation performed on cores retrieved from this basalt. The cross-hole seismic tests were conducted at the U.S. Department of Energy's (DOE) Near-Surface Test Facility (NSTF) located in the northern side of Gable Mountain. Gable Mountain is a tholeiitic basalt outcrop in the north-central portion of DOE's Hanford reserve, 56 kilometers north of Richland, Washington (Figure 1.1). The subsequent laboratory testing was performed on the University of California's Berkeley campus.

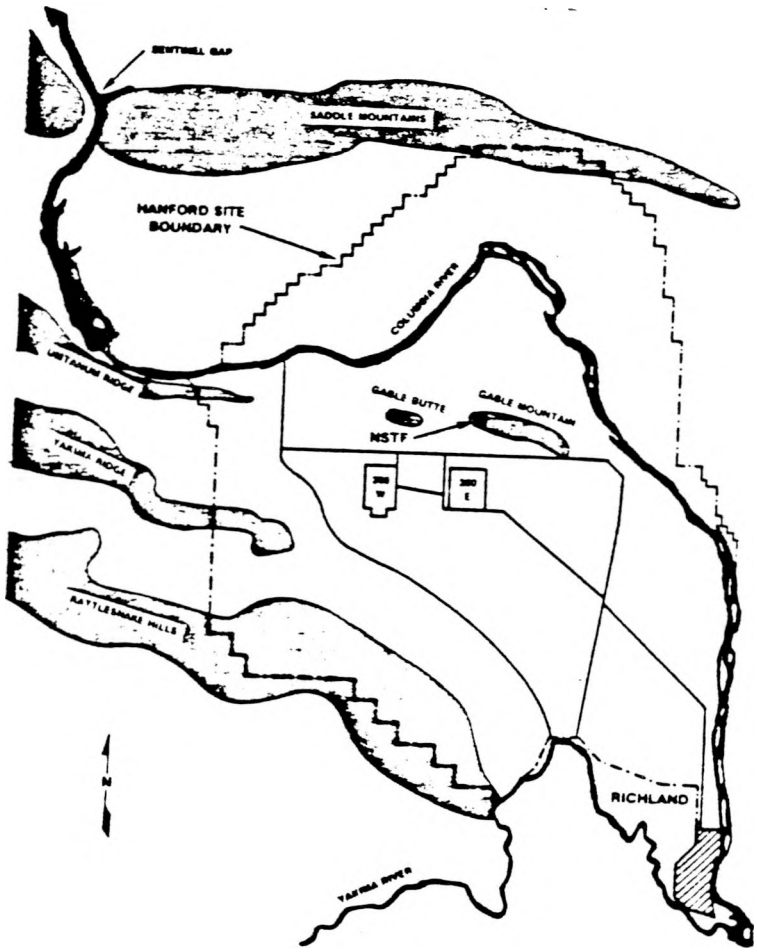

Figure 1.1 Near-Surface Test Facility site location map.

1.2. Objectives

The general objectives of the cross-hole seismic tests were to evaluate the in situ rock mass geomechanical characteristics, and to provide an evaluation of the cross-hole seismic method as a means for anomaly detection. The specific objectives of the study were to:

- Evaluate the compressional (P) and shear (S) wave velocities and their spatial variations within the rock.
- Evaluate the in situ dynamic elastic properties;
  1) Young's modulus
  2) Poisson's ratio

  and their spatial variations.
- Evaluate the P-wave first arrival amplitudes and their spatial variations.
- Analyze the frequency spectra and evaluate the spatial variation in the resulting rock quality factors.
- Identify the disturbed rock zone around the West Access tunnel.
- Assess the spatial variation in fracture density.

The objective of the laboratory core analysis was to supplement the results of the field testing by comparing the geomechanical values obtained in the laboratory under carefully controlled conditions with those obtained in the field.

1.3. Site Geology

The cross-hole tests were performed at the NSTF in the Pomona member of the Saddle Mountain Basalt formation. The NSTF tunnels were excavated by conventional drill-and-blast techniques. The rock in the West Access tunnel (Figure 1.2), where most of the cross-hole measurements were made and the cores retrieved, is reported (Moak and Wintczak, 1980) to consist of dark grey dense basalt with plagioclase lathes. Core logs, provided by Rockwell International, showed that

vesicles occupied 3% of the basalt in the area where the cross-hole measurements were made. The basalt structure was characterized as a flow entablature. The columns were regular but sinuous, ranging from 0.02 to 0.04 meters thick and up to 2.4 meters in length. They dipped from 70 to 90 degrees with no apparent preferred strike direction. These columns were dissected by numerous low-angle discontinuous cross-joints. There was no apparent preferred strike direction to the cross-jointing. The basalt in the Heater Test room, where the remainder of the measurements were made, is generally similar to that in the West Access tunnel with the exception that it was subject to a heating cycle in previous in situ experiments.

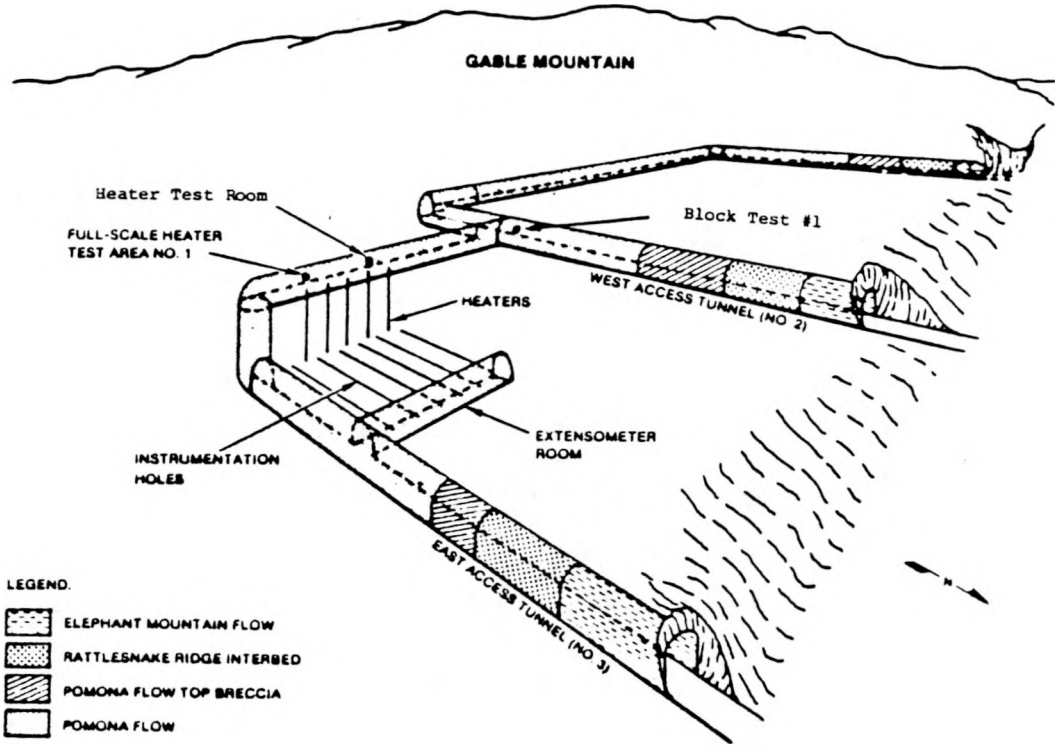

Figure 1.2 Conceptual diagram of the Near-Surface Test Facility.

1.4. Borehole Description

In order to evaluate the geomechanical properties and the blast damage in the rock adjacent the West Access tunnel, Rockwell International provided four parallel diamond-drilled horizontal boreholes centered 6.7 m north of Block Test #1 (Figure 1.3). These boreholes were nominally 76 mm in diameter and penetrated approximately 12 m into the west side of the West Access tunnel. Over-boring, typically 89 mm in diameter, occurred within the first 1.25 m of all four boreholes. Figure 1.4 illustrates an elevation of the tunnel wall containing the four boreholes. The boreholes, labelled C1 through C4, form a diamond pattern with X- and Y- axes of approximately 3 m lengths. The mid-plane of this diamond was under approximately 46 m of overburden. Rockwell International provided survey measurements made within the boreholes that were reported to be accurate to ±5 mm.

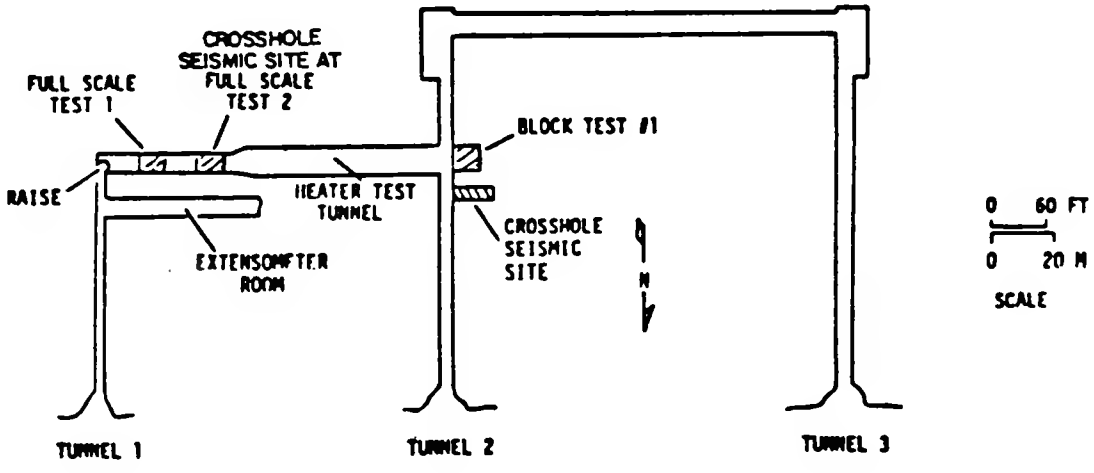

Figure 1.3 Near-Surface Test Facility layout.

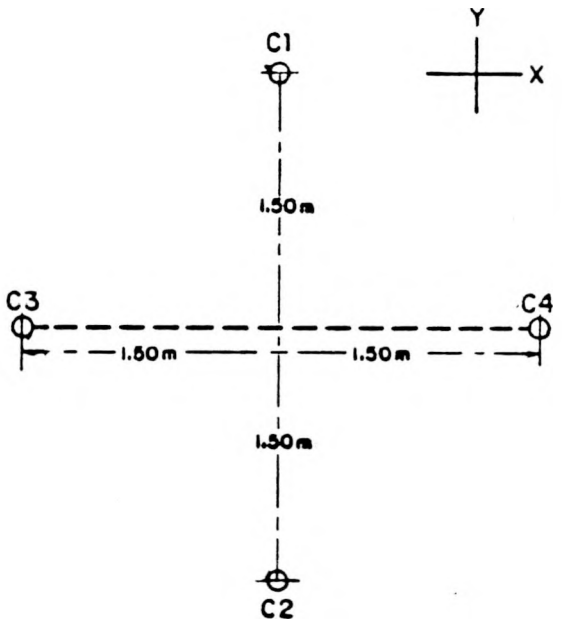

Figure 1.4 Illustration of West Access tunnel wall showing the four horizontal boreholes.

In order to evaluate the geomechanical properties of the rock below the Heater Test room, Rockwell provided three parallel diamond-drilled vertical boreholes in the Heater Test room floor. These boreholes penetrated a minimum of 4.5 m into the tunnel floor and were 76 mm in diameter. Figure 1.5 illustrates the spatial relation between each of the boreholes and the heater used to heat the rock in the previous experiments. Rockwell International also provided survey data accurate to ±5 mm for these boreholes.

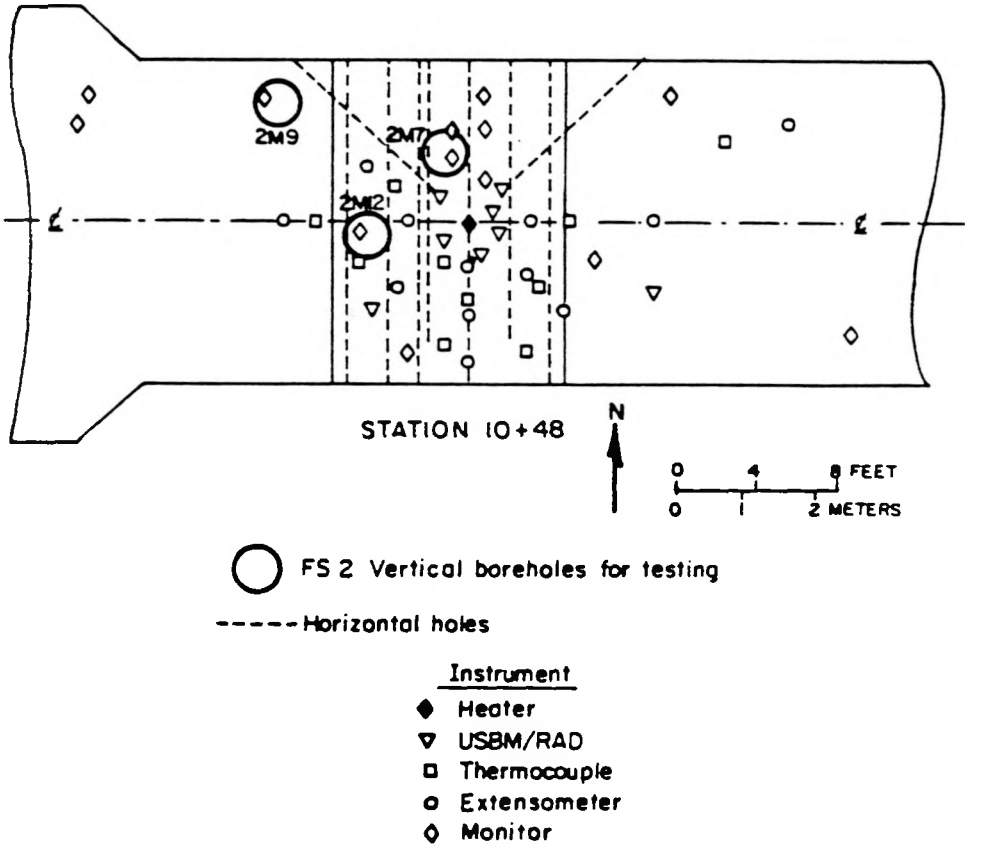

Figure 1.5 Spatial relation between vertical boreholes and heater.

2. Field Testing

2.1. Instrumentation

A schematic diagram of the instrumentation used in the field testing is shown in Figure 2.1. This system is similar in many respects to and developed from the system used for cross-hole seismic testing during the Stripa simulated nuclear waste disposal experiments performed in Sweden (Paulsson and King, 1980). The primary components of the system used at the NSTF are the following:

- Digital oscilloscope, Nicolet model #2090-3, with 12 bit resolution, disk drive, and a 2.0 megahertz sampling capability.
- Direct-drive tape recorder, Hewlett Packard model #3964-A, with a flat frequency response between 300 and 300,000 hertz.
- P- and S-wave transmitting and receiving sondes.
- Selectable gain amplifier, Tektronix model #AM 502, with an adjustable band pass filter.
- High-voltage electrical pulse generator.
- Hydraulic pump.

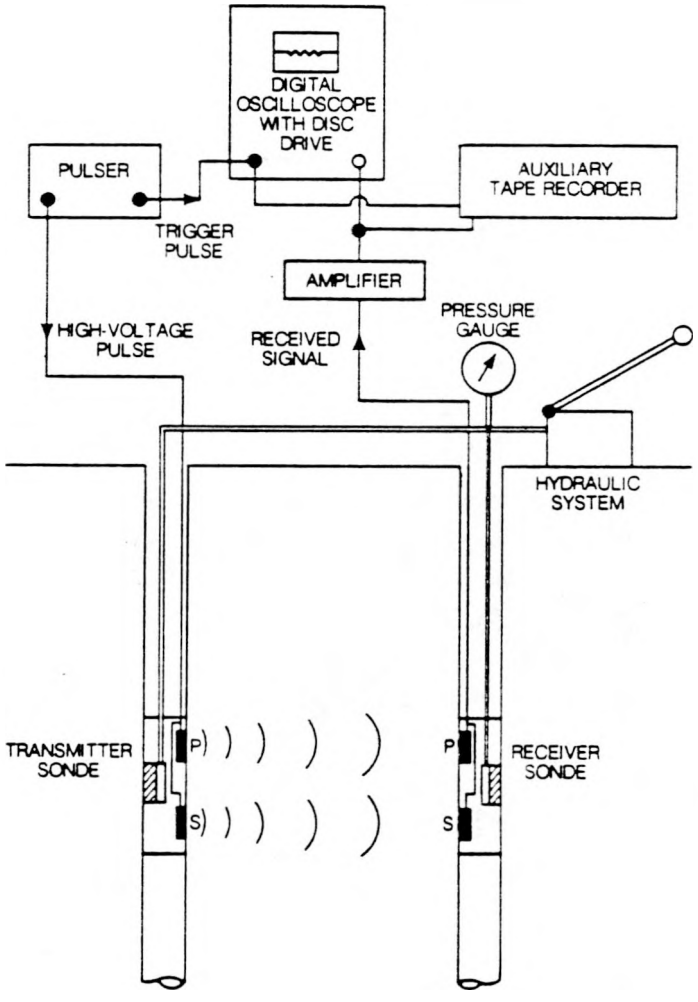

Figure 2.1 Schematic diagram of test equipment.

A cross-section of the sondes containing the piezoelectric P- and S-wave transducers is illustrated in Figure 2.2. The P- and S-wave

piezoelectric crystals are located in the front and rear of the sondes respectively. The transducers are composite ceramic-steel sandwiches approximately 3.5 cm in diameter with S-wave poling across two half disks. The S-wave polarization is parallel to the axes of the sondes. The P- and S-wave signals produced from the crystals have flat frequency responses between 1 and 50 kilohertz.

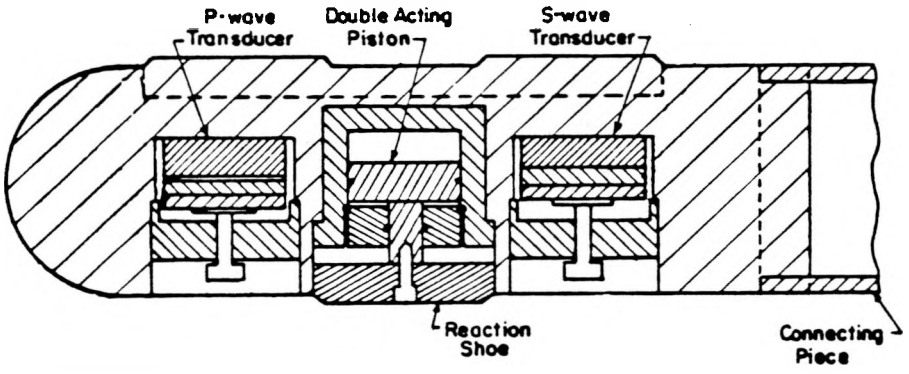

Figure 2.2 Sonde cross section.

A reaction shoe connected to a double-acting hydraulic cylinder is located between the two crystals. The reaction shoe is used to force the sonde against the borehole walls, coupling it to the rock. The double acting cylinder allows the reaction shoe to be both retracted as well as

extended by the hydraulic pump.

Hydraulic and electrical connections are made inside a hollow connecting piece attached to the rear of the sondes. Two preamplifiers are located in the receiving sonde's connecting piece. These are used to amplify the signal by 40 decibels and to drive the cable before transmission to the Tektronix amplifier. The shielded power cables from the high-voltage pulse generator are connected directly to the transmitting P- and S-wave crystals.

Two segmented rods are used to position the sondes in the boreholes. These rods connect to the back of the connecting pieces. Each of the rods' segments are 2.0 m long and are coupled together in such a way that the orientations of the sondes are known at all times. The rods are marked at 1.0 m intervals. Using a meter stick and these meter marks, the sondes can be positioned with 0.5 cm accuracy within boreholes.

2.2. Measurement Locations

Five hundred and eighty-eight measurements were made between the four horizontal boreholes located near BT#1. With the transmitting sonde in one borehole and the receiving sonde in another, six different travel path orientations lying in vertical planes were made from the four boreholes: one in the vertical direction, one in the horizontal, and four along diagonal paths 45 degrees from the vertical. Borehole designations for the transmitter and receiver are listed in Table 2.1.

Table 2.1
Borehole designations for the transmitter and receiver in the four vertical boreholes

	Borehole					
Transmitter	C2	C3	C4	C3	C3	C2
Receiver	C1	C1	C1	C2	C4	C4

A total of 24 measurements were taken between the three vertical boreholes in the floor of the Heater Test room. From these three boreholes, three travel path orientations lying in horizontal planes were made. Borehole designations for the transmitter and receiver are listed in Table 2.2.

Table 2.2
Borehole designations for the transmitter and receiver in the three verticle boreholes

	Borehole		
Transmitter	2M9	2M9	2M12
Receiver	2M7	2M12	2M7

Before a series of measurements was made between the four horizontal boreholes, the sondes were inserted into their designated boreholes to predetermined stations. Except near the borehole collars, these stations were defined by 20 vertical planes parallel to the tunnel axis. Figure 2.3 illustrates a typical station and its six associated travel paths. The lengths of the travel paths were calculated from the survey data and are listed in table A.2. The travel path lengths are accurate to ±5 mm. When a measurement was taken at a particular station, the sondes were parallel to each other and the travel paths were at right angles to the axes of the boreholes. Due to tunnel curvature, the four borehole collars did not lie in a vertical plane. This necessitated the use of an additional four stations lying in non-vertical planes (Figure 2.4).

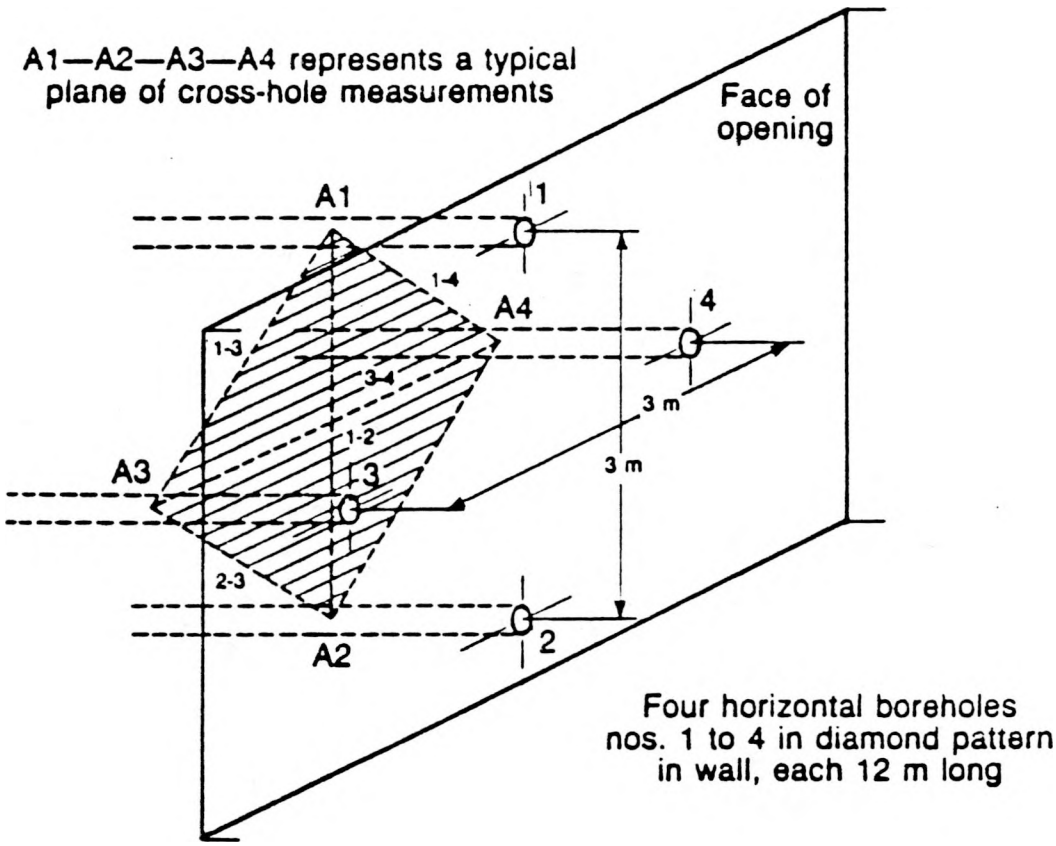

Figure 2.3 Typical measurement station and associated travel paths.

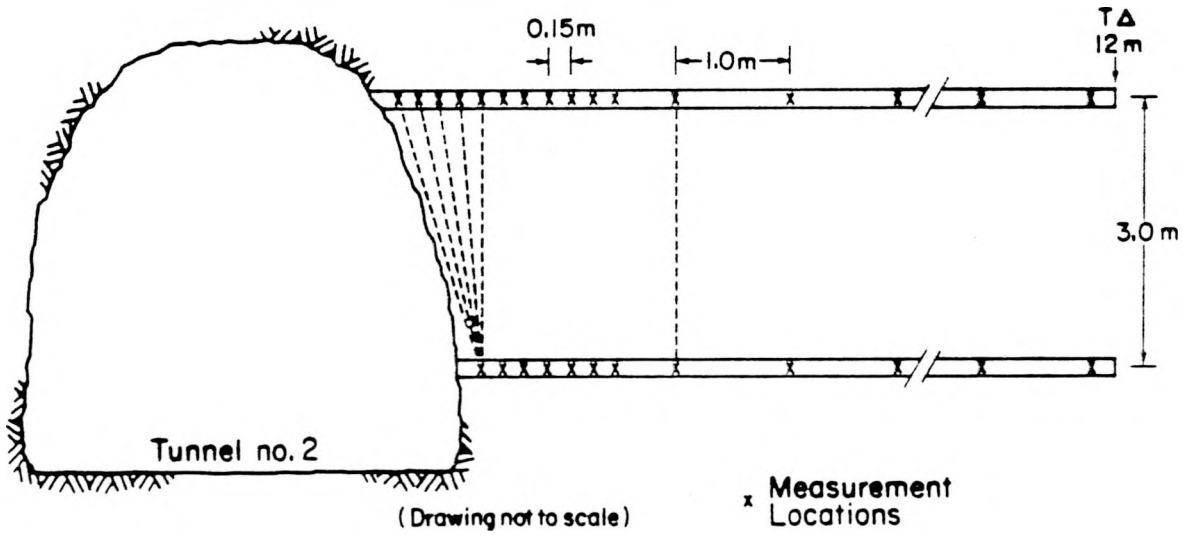

Figure 2.4 Additional stations lying in non-vertical planes.

With respect to the collar of borehole C2, the vertical planes of the measuring paths were located at 15 cm intervals for the first 1.2 m into the borehole. A station was located at 1.5 m, and from 2.0 m to 11.0 m into the borehole, stations were located at 1.0 m intervals (Figure 2.5). Some of the borehole combinations at a given station were omitted because of irregularities in the diameters of one or both borehole walls. Table A.1 lists the stations and their respective distances from each of the borehole collars.

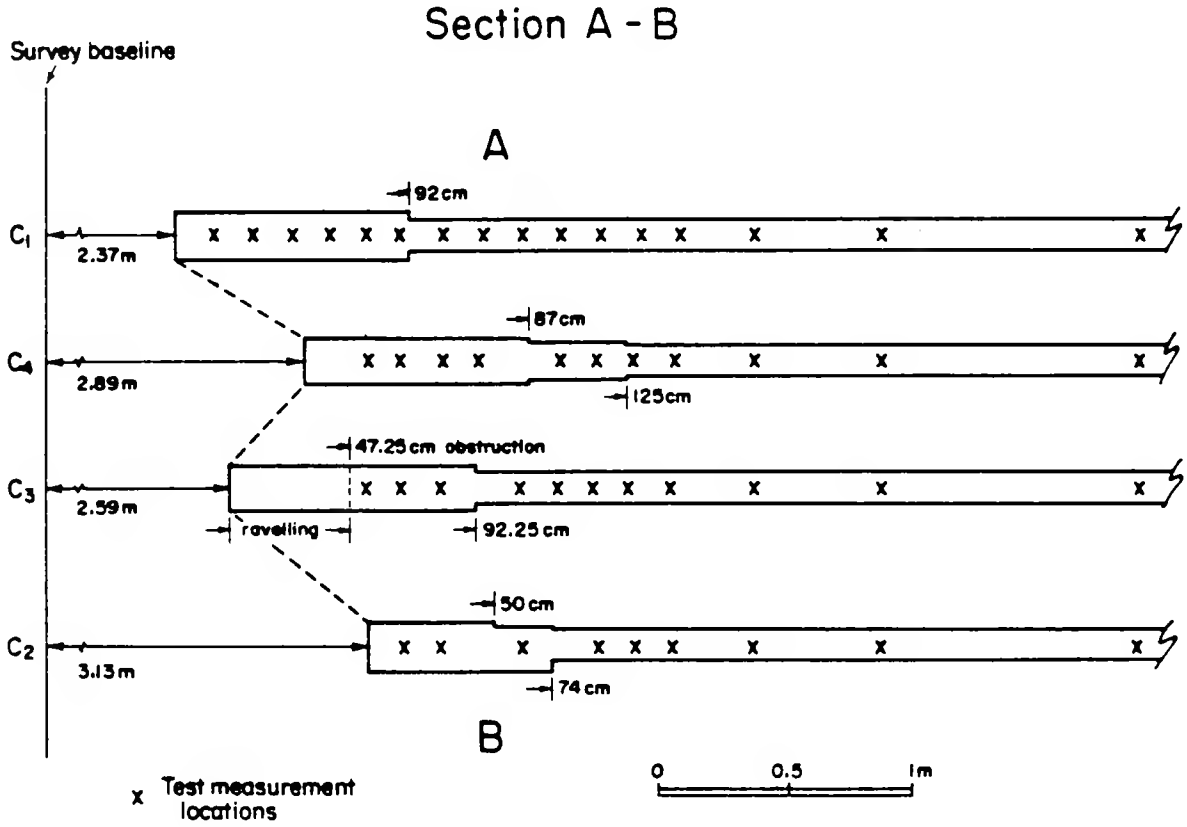

Figure 2.5 Measurement locations used in the horizontal boreholes.

Only two stations, each containing three travel paths, were used in the three vertical boreholes (prescribed by Rockwell International). They

were defined by horizontal planes 3.0 and 4.25 m below the Heater Test room floor. Their respective distances from each of the three borehole collars are listed in Table A.1, and the lengths of the six travel paths are listed in Table A.3.

2.3. Wave Transmission and Capture

Once the sondes were positioned at a particular station, they were forced against the sides of the boreholes with the hydraulic system and reaction shoes. Because signal attenuation is sensitive to the quality of the coupling between the rock and the sondes, care was taken to insure that the same hydraulic line pressure, 103 MPa, was used during each measurement. In the 76 mm diameter boreholes, 103 MPa of line pressure resulted in approximately 3.5 MPa of normal stress between the bearing pads of the sondes and the borehole walls. The curvature of the bearing pads was designed to match the curvature of the 76 mm boreholes. Therefore, when the diameter of the boreholes exceeded 76 mm, the normal stress between the sonde and rock increased as the area of contact between was reduced. The uneven coupling stresses, which may have occurred in the larger diameter sections of the boreholes, may have affected the signal attenuation measurements presented later in this report.

Once the sondes were coupled to the borehole walls, a measurement was made as follows. The pulse generator was triggered and two simultaneous electrical pulses were generated; a high-voltage pulse which was conveyed to one of the two transmitter piezoelectric crystals, and a low-voltage pulse with a short rise time which was used to trigger an oscilloscope sweep. The high-voltage pulse caused a single seismic wavetrain,

either a P- or S-wave, to be propagated from the transmitting sonde. This wave traveled through the rock and then was sensed by the corresponding crystal in the receiving sonde. The signal was amplified first in the receiving sonde's preamplifier and again in the Tektronix amplifier, located in the drift, before being displayed on the sweep of the oscilloscope. The gain of the Tektronix amplifier was adjusted to take best advantage of the resolving power of the digital oscilloscope. The bandwidth of the Tektronix amplifier was set to provide uniform gain for frequencies between 1 and 300 kHz.

The oscilloscope was set to record at a 1.0 MHz (1.0 μs) sampling rate with a total of 4096 samples taken per sweep. A sweep was retained on the CRT of the oscilloscope until a new sweep was generated. Typically the seismic wavetrain generated by the transmitting piezoelectric crystal arrived 400 μs after the start of a sweep. A number of signals would be generated between each borehole pair at each station. When it was determined that the cultural noise contained in the trace prior to the P- or S-wave arrival had the lowest attainable amplitude, the trace was stored on a floppy disk. Therefore, even though a large number of seismic waves may have been generated between two boreholes at a given station, only two of each type of wave were saved for analysis.

At some stations, particularly near the borehole collars, the signal amplitudes had attenuated to the level of the cultural noise. At these stations, the pulser was set to produce repetitive pulses at 33 ms intervals, and the resulting waveforms were recorded on the Hewlett Packard tape recorder. The repetitive signals could then be played back through an oscilloscope and, where possible, the first-arrival times were determined.

2.4. Repeatability

Measurements were repeated at certain stations between boreholes C1 and C2, C1 and C3, and C2 and C4. For these measurements, stations measured previously were reoccupied and measurements were again made. The percent differences between the original measurements and the repeated measurements were averaged for each of the geomechanical parameters tested and are listed in Table 2.3. The value ranges listed in Tables 2.4 through 2.7 were derived from the values listed in Table 2.3.

Table 2.3
Average percent differences between original and repeated measurements.

Parameter	% Difference
P-wave Velocity	2.8%
S-wave Velocity	2.5%
Young's Modulus	5.0%
Poisson's Ratio	5.0%
Arrival Amplitude	90.0%
Rock Quality Factor	23.0%

2.5. P- and S-waveforms

Figures 2.6 through 2.9 represent typical waveforms and their Fourier amplitude spectra. Figure 2.6 shows a typically good pair of signals that were measured between boreholes C1 and C2 at station 16. The first arriving P- and S-wave wavelets'[1] Fourier amplitudes peaked at approximately 30 and 26 kilohertz respectively (Figure 2.7). A poor set of signals measured between boreholes C3 and C4 again made at station 16 are shown in figure 2.8. The peak Fourier amplitudes for the first arriving

[1] Because it was assummed that multiple arrivals and mode conversion would contaminate all but the first complete cycle of the P-waves, only this cycle, usually 70 μs long, was used to obtain thier Fourier amplitude spectra.

wavelets for these signals occurred at less than 2 kilohertz (Figure 2.9).

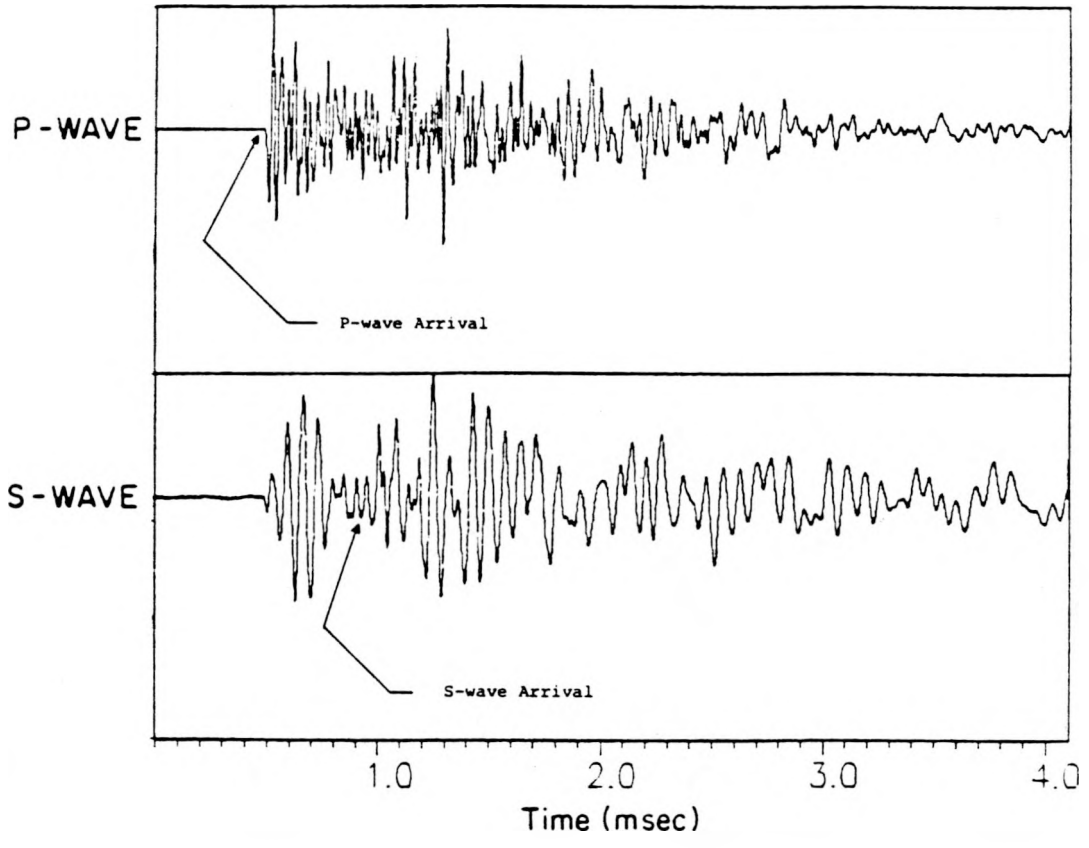

Figure 2.6 A typical set of the better quality P- and S-waves.

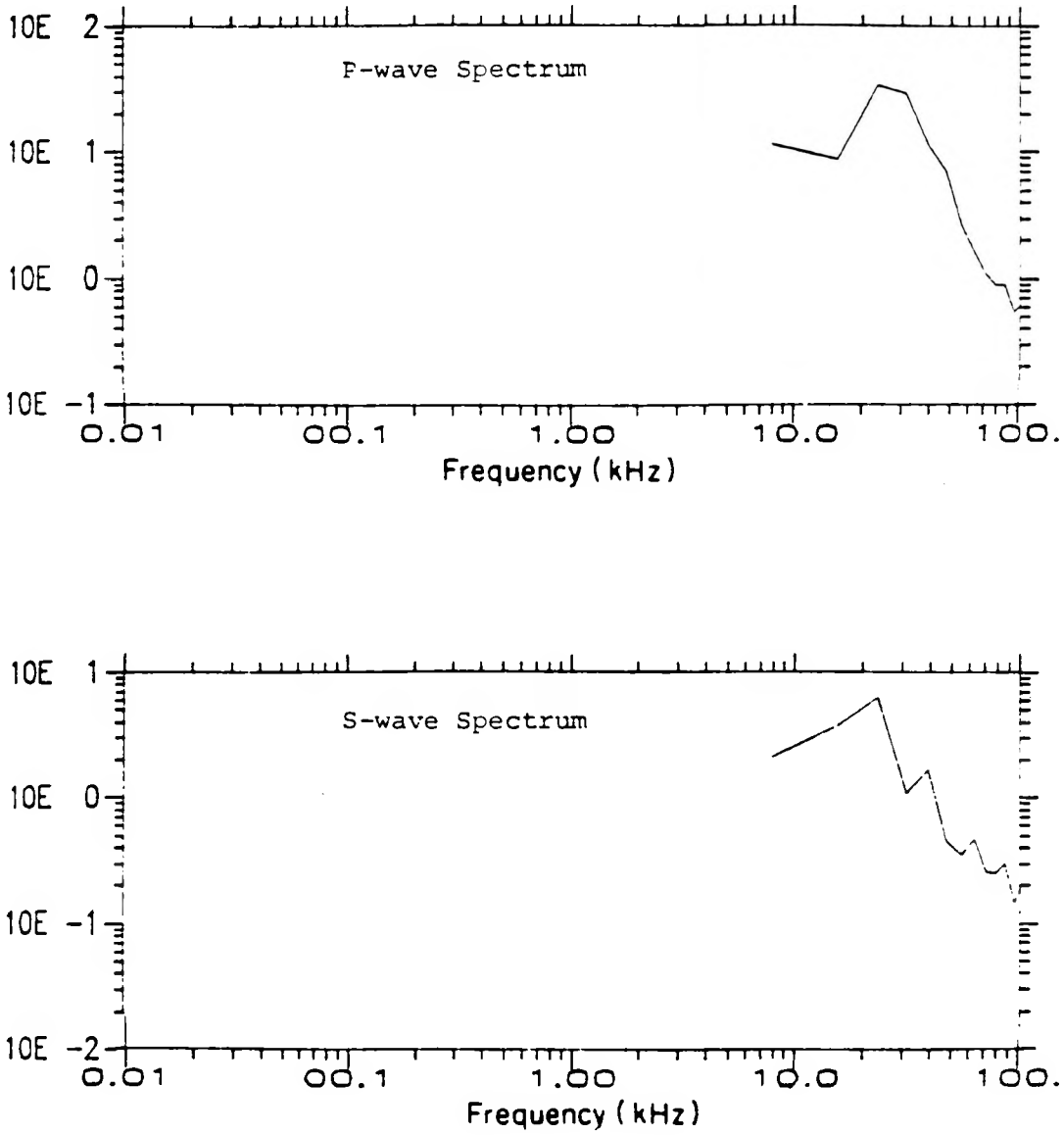

Figure 2.7 Spectra for waveforms illustrated in Figure 2.6.

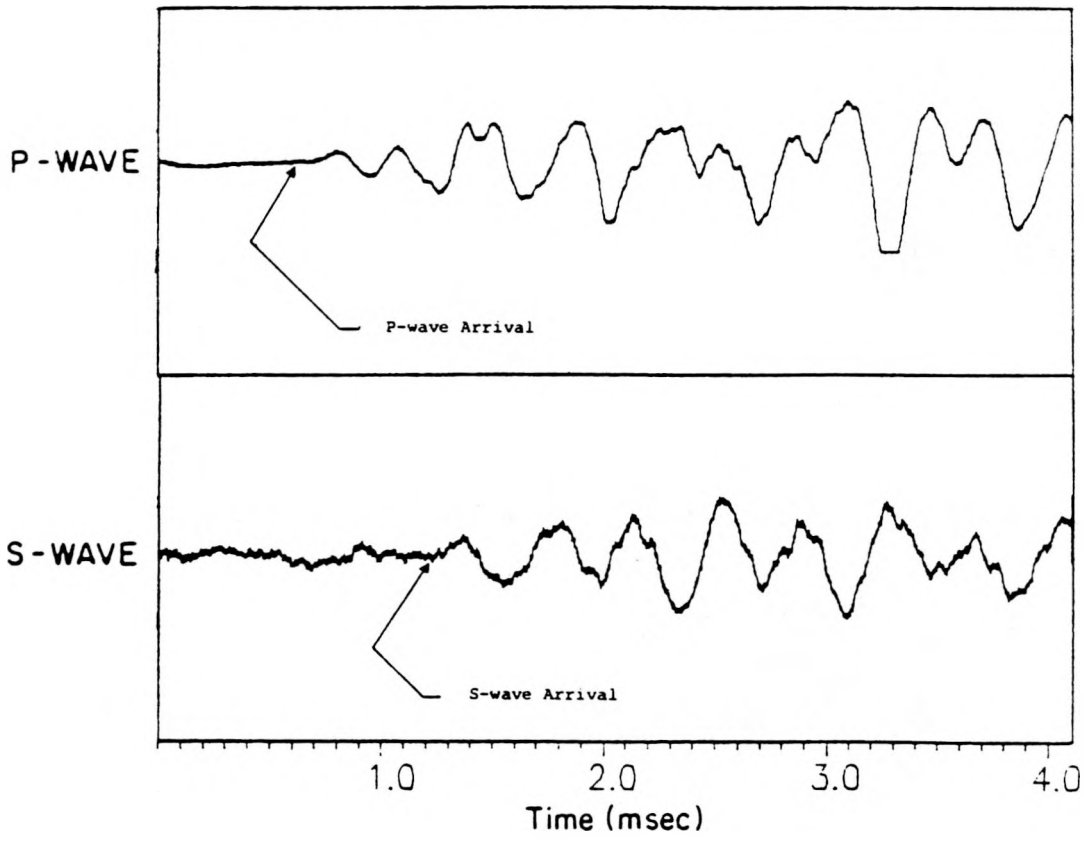

Figure 2.8 A typical set of the poorer quality waves.

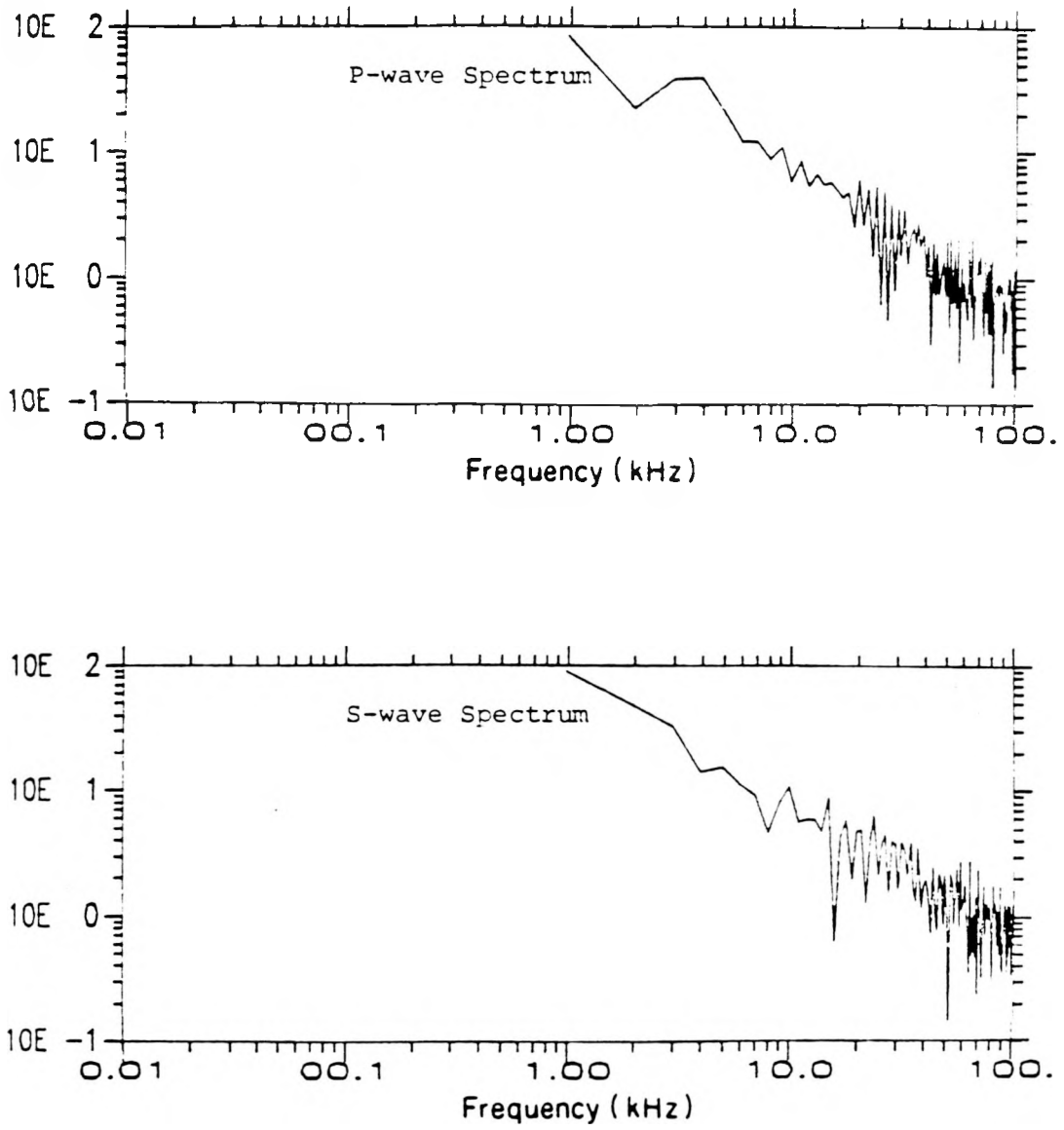

Figure 2.9 Spectra for waveforms illustrated in figure 2.8.

2.6. Velocity Determinations

The first step in determining the in situ P- and S-wave velocities for the basalt was to determine the first arrival times. These are the times on the oscilloscope traces where the arriving seismic wavetrains could first be distinguished from the cultural and system background noise. The P-waves had a distinctive trough (Figure 2.10) that occurred at the begining of the wavetrain. This trough had an amplitude several times greater than the background noise, making picking of the P-wave first arrivals straightforward. The S-wave first arrivals were more difficult to determine. Mode conversion of S-waves to P-waves occurred during most of the S-wave measurements. Due to their greater velocities, these P-waves would arrive before and simultaneously with the S-waves (Figure 2.10) making the picking of a first arrival difficult in some traces. From the well defined P-wave first arrivals and the relationship between P- and S-wave velocities for a reasonable range of Poisson's ratio, the earliest and latest possible S-wave arrival times could be determined. If Poisson's ratio was assumed to be between 0.20 and 0.35, these times formed a window approximately 30.0 μs long. A trace of the pilot signal was compared with the trace containing the S-wave, and the most plausable first arrival within the arrival window was found. The P-wave arrivals showed that the velocities did not vary significantly between two consecutive stations within the same borehole pair. Therefore, it was assumed that the S-waves first arrivals also had to be consistant between two consecutive stations, thus eliminating more of the ambiquity in picking S-wave first arrivals. However, it is possible that some of the S-wave first arrival times are in error by 5% to 15%.

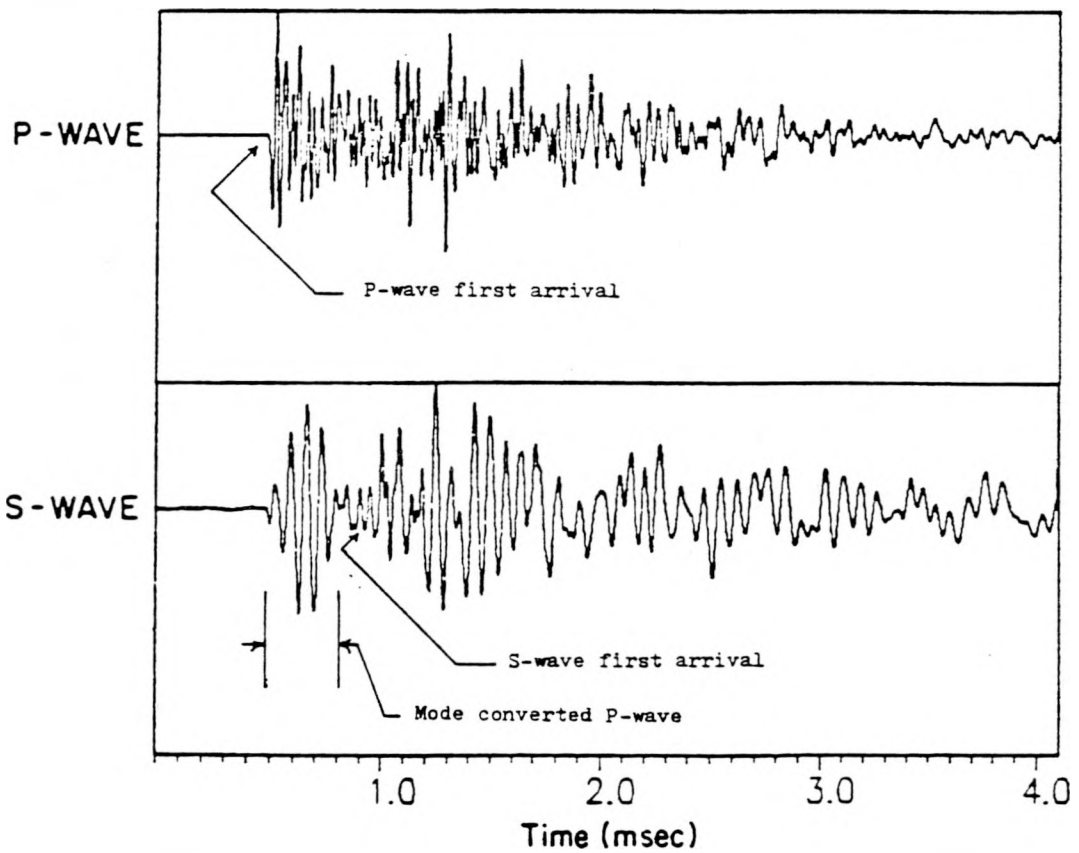

Figure 2.10 First arrivals for the P- and S-waves.

Once the first arrival times were determined, the time the signals spent in the sondes had to be accounted for. These delay times were

found by placing an aluminum block of known dimensions between the sondes and measuring the transit time for the seismic signals (Figure 2.11). Assuming P- and S-wave velocities within the aluminum of 6248 and 3109 m/s respectively (King, 1966), the delay times were calculated to equal 19.5 and 35.6 μs respectively.

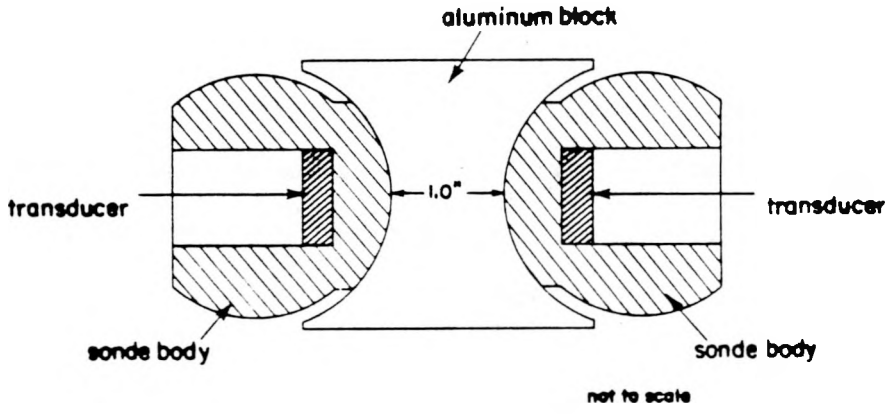

Figure 2.11 Aluminum block used to determine the instrument delay times

With travel path lengths calculated from the survey data provided by Rockwell and the corrected travel times, the in situ P- and S-wave velocities were determined for the basalt. The equation used for calculating the velocities is:

$$V = D / T \qquad (2.1)$$

V = *velocity*

D = *distance*

T = *arrival time*

The P- and S-wave velocities for the six different travel path orientations between the four horizontal boreholes are listed in Table A.2 and are illustrated in Figures 2.12 and 2.13. Figure 2.12 shows the relationship between velocity and position for boreholes C1 and C2, and C3 and C4. The velocities measured in the vertical travel paths between C1 and C2 are typically 800 to 1000 m/s higher than in the horizontal travel paths between C3 and C4. It has been shown that the more jointed a rock is, the slower seismic waves travel through it (O'Connell and Budiansky, 1977; Hadley, 1976). Therefore, these data appear to indicate that waves traveling in the vertical travel paths intersect fewer fractures than those traveling in horizontal travel paths. This is consistant with the columnar jointing found in this basalt.

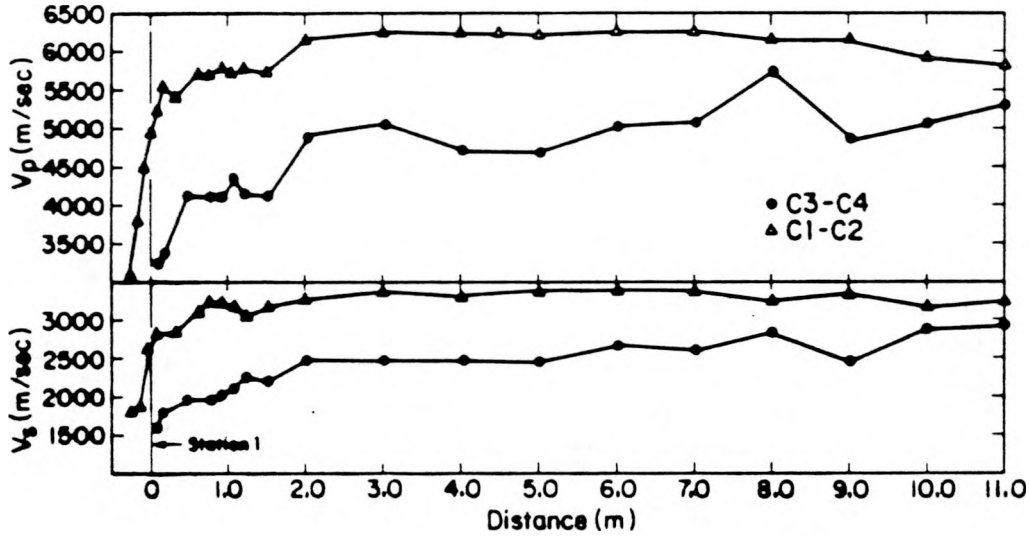

Figure 2.12 P- and S-wave velocities for the vertical and horizontal travel paths

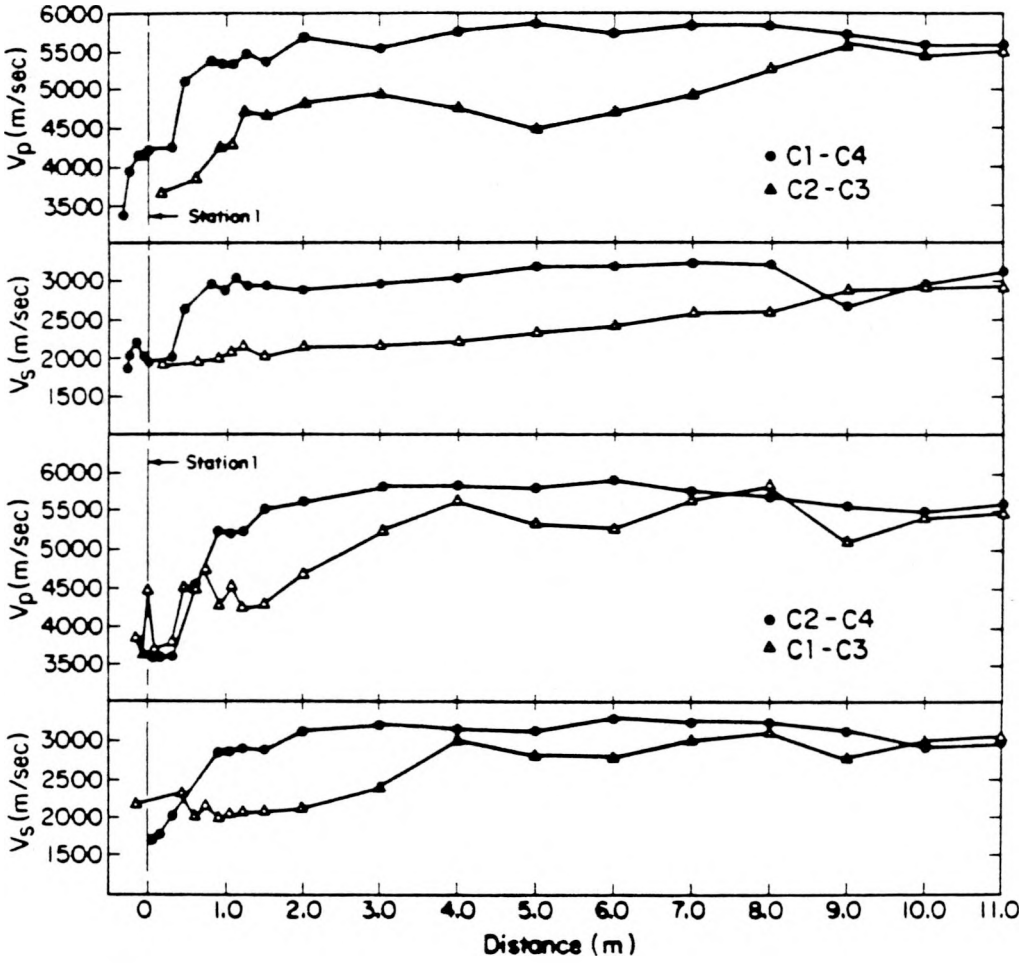

Figure 2.13 P- and S-wave velocities for the diagonal travel paths.

Figure 2.13 shows the relation between velocity and position for the four diagonal travel paths. If a uniform rock matrix between fractures is

assumed, and had the columnar and low-angle discontinuous jointing been uniform in density throughout the rock, waves traveling through these diagonal travel paths would have intersected the same number of fractures and would have the same velocities. This appears not to have been the case. Table 2.4 lists the average velocities for the last 11 stations for each of the diagonal travel paths in descending order[2]. The velocities for the travel paths between boreholes C2 and C4 are the greatest while those between C2 and C3, the lowest. The rock between C2 and C4 appears to have the least overall number of joints while the the rock between C3 and C2, the most. Although data error could have been responsible for the variations in these velocities, all the rest of the parameters to be presented in the thesis also show this relation.

Table 2.4
Average P- and S-wave velocities for the last 11 stations for the diagonal travel paths.

Borehole Pair	P-wave Vel. (m/s)	S-wave Vel. (m/s)
C2-C4	5705 ± 160	3129 ± 78
C1-C4	5658 ± 158	3049 ± 76
C3-C1	5265 ± 147	2814 ± 70
C3-C2	4965 ± 139	2492 ± 62

The velocities for all six travel paths decrease as the borehole collars are approached. Typically the decrease is first observed 1.5 m into the rock. These decreases in velocity appear to be indicative of an increased fracture density near tunnel walls due to the blasting used in mining the tunnel. This represents the disturbed rock zone. It appears that the disturbed rock zone is confined to the first 1.5 m of rock

[2] Because the blast damage zone was found to affect the geomechanical rock properties determined from the first nine stations, these stations were omitted when averages were obtained. To obtain averages for the P-wave first arrival amplitudes and relative Q values, the $\log_{10}$ of these values was first calculated. Averages were than obtained from these logs.

adjacent to the tunnel opening.

The velocities measured between the three vertical boreholes in the Heater Test room floor are listed in Table A.3. The average P-wave velocity for these boreholes, 2609 m/s (± 65), is from 2000 to 3500 m/s lower than the average P-wave velocities found between the four horizontal boreholes. The average S-wave velocity, 1352 m/s (± 33), is from 1100 to 2000 m/s lower than the average S-wave velocities found between the four horizontal boreholes. The velocities for the travel paths closest to the heater used in previous heater experiments, between boreholes 2M12 and 2M7, are remarkably low. Velocities observed between 45 cm diameter boreholes in this area prior to the time when the rock was subject to a thermal cycle were reported to be 5469 and 2948 m/s for the P- and S-waves respectively (Moak and Wintczak, 1980). The velocities currently measured indicate the rock is considerably more fractured than it was before the thermal cycle. Because signal attenuation may have caused the first arriving wavelets to be overlooked, and only 24 measurements were made and none were repeated, it is possible that error could exist in the data. More measurements would need to be taken to insure the conclusion regarding increased fracturing was indeed valid.

2.7. Dynamic Elastic Moduli

The equation for determining the dynamic Poisson's ratio from the P- and S-wave velocities is (Jaeger and Cook, 1976):

$$\nu = \frac{(\alpha^2 - 2)}{2(\alpha^2 - 1)} \qquad (2.2)$$

ν= *Poisson's Ratio*

$\alpha = \frac{V_p}{V_s}$

V_p = *P—wave velocity*

V_s = *S—wave velocity*

Once Poisson's ratio is derived, the equation for determining the dynamic Young's modulus from the velocities is (Jaeger and Cook, 1976):

$$E = \rho V_p^2 \frac{(1+\nu)(1-2\nu)}{(1-\nu)} \qquad (2.3)$$

ρ= *rock density* (2848 kg/m^3 for *this rock mass*)

E = *Young's Modulus*

Using these two equations, the dynamic rock moduli were calculated for each borehole pair at each station. The value for the rock density used here, 2848 kg/m^3, was an average for 248 rock samples taken from the Pomana entablature (Schmidt, 1980). The values for Poisson's ratio and Young's modulus are listed in Table A.2, and their relations between borehole pairs and position are illustrated in Figures 2.14 and 2.15.

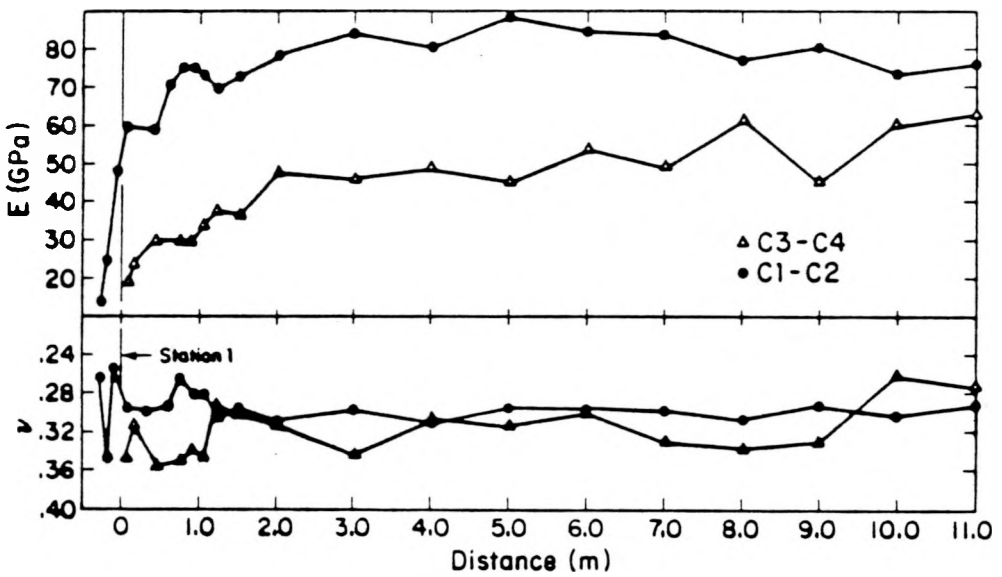

Figure 2.14 Dynamic Young's moduli and Poisson's ratios for the vertcal and horizontal travel paths.

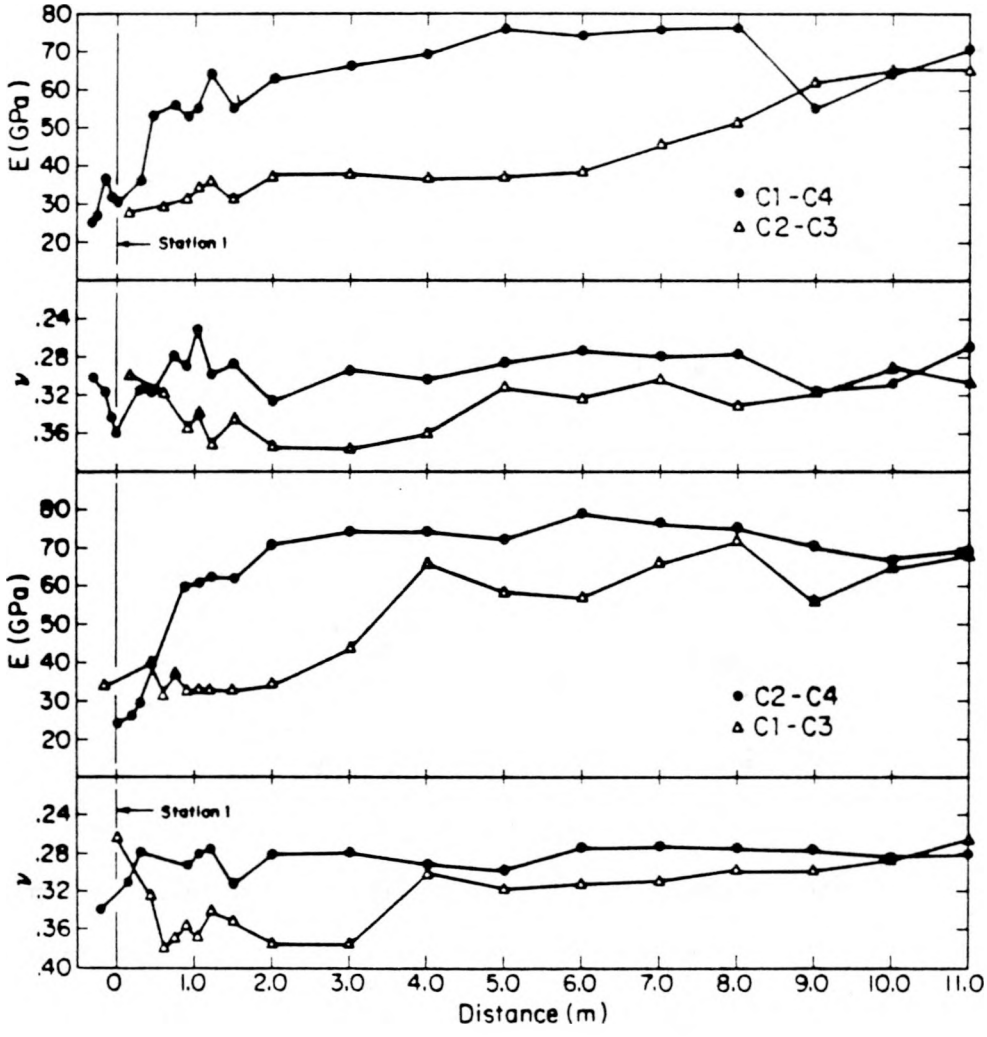

Figure 2.15 Dynamic Young's moduli and Poisson's ratios for the four diagonal travel paths.

The average value of Poisson's ratio for the last 11 stations in the vertical travel paths was 3.3% higher than for the horizontal travel paths. This is within the estimated error of 5% (Table 2.3), but it has been shown

that Poisson's ratio will increase with increased fracture density if the rock is saturated[3] (O'Connell and Budiansky, 1977).

Table 2.5 lists the average values of Poisson's ratio for the last 11 stations for the four diagonal travel paths in ascending order. The lowest average value was measured between boreholes C2 and C4, and the greatest between boreholes C3 and C4. These values again appear to indicate that travel paths between C2 and C4 intersect fewer joints than travel paths between C3 and C2.

Table 2.5
Average Young's modulus and Poisson's ratio for the last 11 stations for the diagonal travel paths.

Borehole Pair	Young's Modulus (10^9 Pascals)		Poisson's Ratio	
C2-C4	72	± 4	0.28	± .02
C1-C4	68	± 4	0.29	± .02
C3-C1	56	± 3	0.32	± .02
C2-C3	48	± 2	0.33	± .02

As measurements were made near the borehole collars, in the disturbed rock zone, the increased fracture density was expected to increase the values for Poisson's ratio. However, the values for Poisson's ratio did not increase as the borehole collars were approached. The laboratory data to be presented later in this thesis showed that the P-wave velocities tended to decrease more rapidly than the S-wave velocities when the axial stress was reduced. At the low confining stresses near the tunnel wall, the P-wave velocities should also have tended to decrease more rapidly than the S-wave velocities. Because Poisson's ratio as calculated from equation 2.2 is a function of V_p / V_s, it should

[3] A discussion of the possible saturation states of the rock directly adjacent the West Access tunnel and below the Heater Test room floor is given with the laboratory results.

have tended to decrease at low confining stresses. Conversely, the increased fracture density would have tended to raise Poisson's ratio. These conflicting factors probably account for the fact that no discernable trend was found in the Poisson's ratios as the borehole collars were approached.

Young's moduli for the vertical travel paths are approximately 32 GPa higher than for the horizontal travel paths. This indicates that the rock is more stiff in the vertical direction than in the horizontal, consistant with the columnar characteristics of the basalt. O'Connell and Budiansky (1977) showed that Young's Modulus will decrease with an increase in fracture density. The average values for Young's moduli for the four diagonal paths follow the same trends as the data thus far presented (Table 2.5). Young's moduli are greatest between boreholes C2 and C4, and least between boreholes C3 and C2, indicating that the rock is less stiff and presumably more jointed between the latter borehole pair. Young's moduli also decrease as the borehole collars are approached, begining 1.5 m into the tunnel wall. This indicates that the damaged rock zone is confined within the first 1.5 m of rock adjacent to the tunnel.

Poisson's ratio and Young's moduli for the three vertical boreholes are listed in Table A.3. Poisson's ratio varies between 0.22 and 0.36, and averages 0.29 (±.02). O'Connell and Budiansky (1977) showed that Poisson's ratio will be reduced with increased jointing if the rock is dry; the travel paths closest to the heater have the lowest Poisson's ratios. Young's moduli are from 20 to 80 GPa lower between these three boreholes than between the four horizontal boreholes near BT#1. The lowest values were found in the travel paths closest to the heater, between borehole 2M12 and 2M7. Prior to the heating cycle experiments,

Young's modulus measured by a static technique in this area was reported to range between 69.8 and 88.8 GPa (Duvall and others, 1978). The average dynamic value of Young's modulus found during the current tests, 1.6 GPa (±.08), is greater than an order of magnitude less than static value measured prior to the thermal experiments. These data indicate that the rock below the Heater Test room floor is much less stiff than the rock adjacent to the West Access tunnel and apparently much less stiff than it was prior to the heating cycle.

2.8. First Arrival Amplitudes

The amplitudes of the first arriving wavelets were studied to determine the signal attenuation properties of the rock. Figure 2.16 illustrates a P-wave and its associated first arriving wavelet. To determine the first arrival amplitudes, the amplitude of the first trough was measured on the oscilloscope screen and divided by the gain of the Tektronix amplifier. Note that this procedure does not take into account the period of the first arriving wavelet. Table A.2 lists the first arrival amplitudes for the various pairs of boreholes at different stations. Because of interference between the mode-converted P-waves which arrived simultaneously with the S-waves, the arrival amplitudes for the S-waves could not be determined.

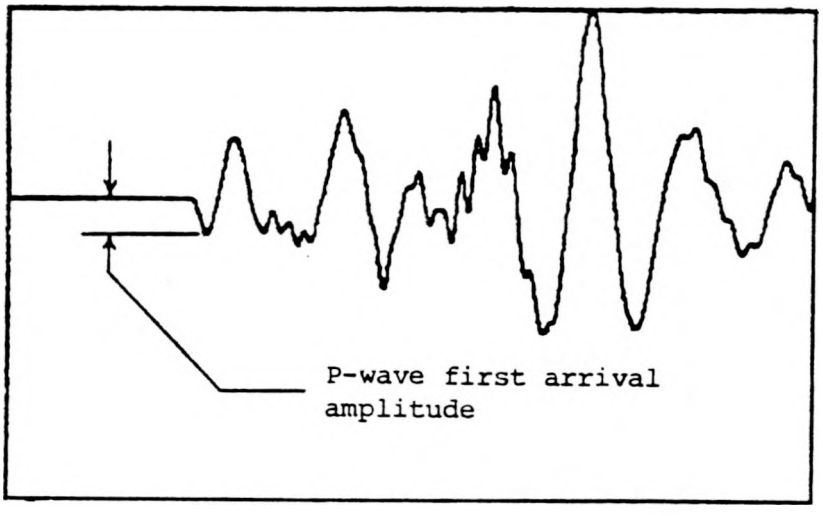

Figure 2.16 Measurement of the amplitude of the first arriving trough.

Figure 2.17 illustrates the first arrival amplitudes for the vertical and horizontal travel paths at different stations. The average first arrival amplitude for the vertical paths is roughly an order of magnitude greater than for the horizontal paths. O'Connell and Budiansky (1977) have shown that an increase in fracture density will cause an increase in signal attenuation. Therefore, these data are interpreted as indicating that

waves traveling along vertical travel paths intersect fewer fractures and are therefore less attenuated than waves traveling along horizontal travel paths. There is also a tendency for the amplitudes to decrease as the borehole collars are approached. This tendency is not as well defined as it is with the other geomechanical properties previously presented, probably because of the inconsistent coupling pressures that occurred in the oversized sections of the boreholes. These data are again indicative of a columnar jointed rock with a greater fracture density occurring near the tunnel opening.

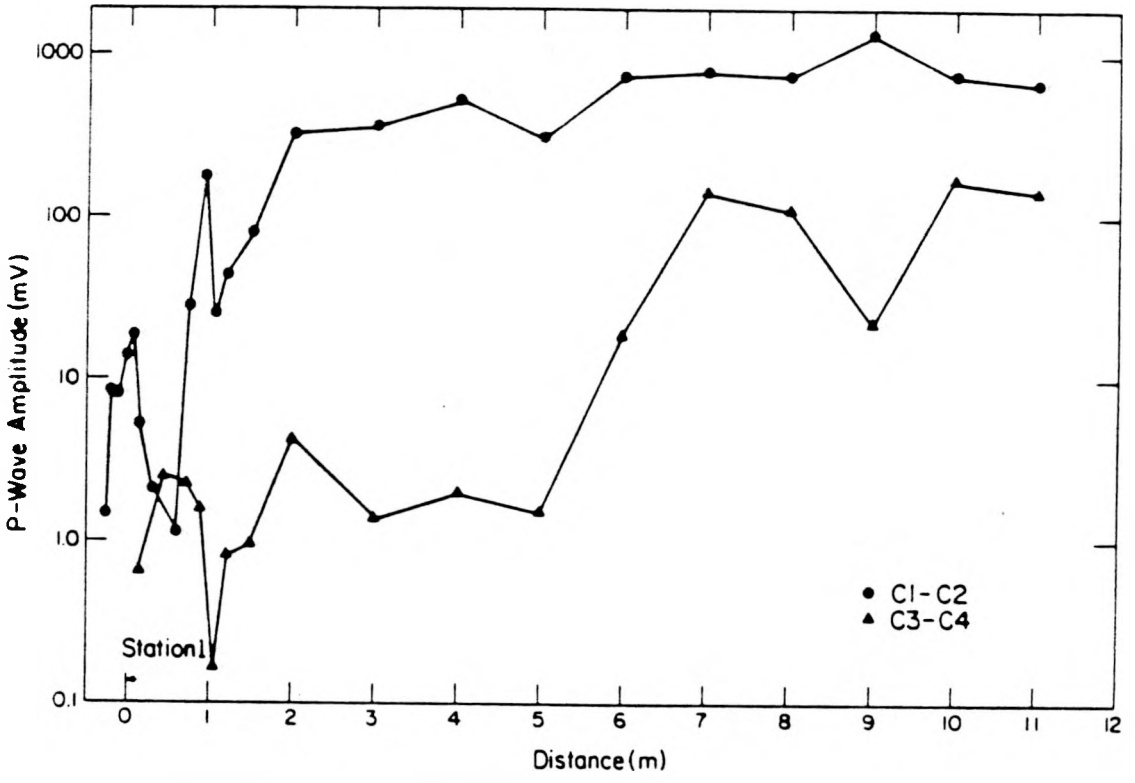

Figure 2.17 First arrival amplitudes for the vertical and horizontal travel paths

Table 2.6 lists the average first arrival amplitudes for the four diagonal travel paths (Figure 2.18) in desending order. This order is the same as that for velocity, Young's modulus, and Poisson's ratio. Waves traveling

between boreholes C2 and C4 had greater first arrival amplitudes than waves traveling between C3 and C2. The density of fracturing again appears to be greater between the latter borehole pair.

Table 2.6
Average first arrival amplitudes for the last 11 stations for the diagonal travel paths

Borehole Pair	Amplitude (mV)
C2-C4	97 ± 87
C1-C2	36 ± 59
C3-C1	1.9 ± 2.1
C3-C2	1.2 ± 1.2

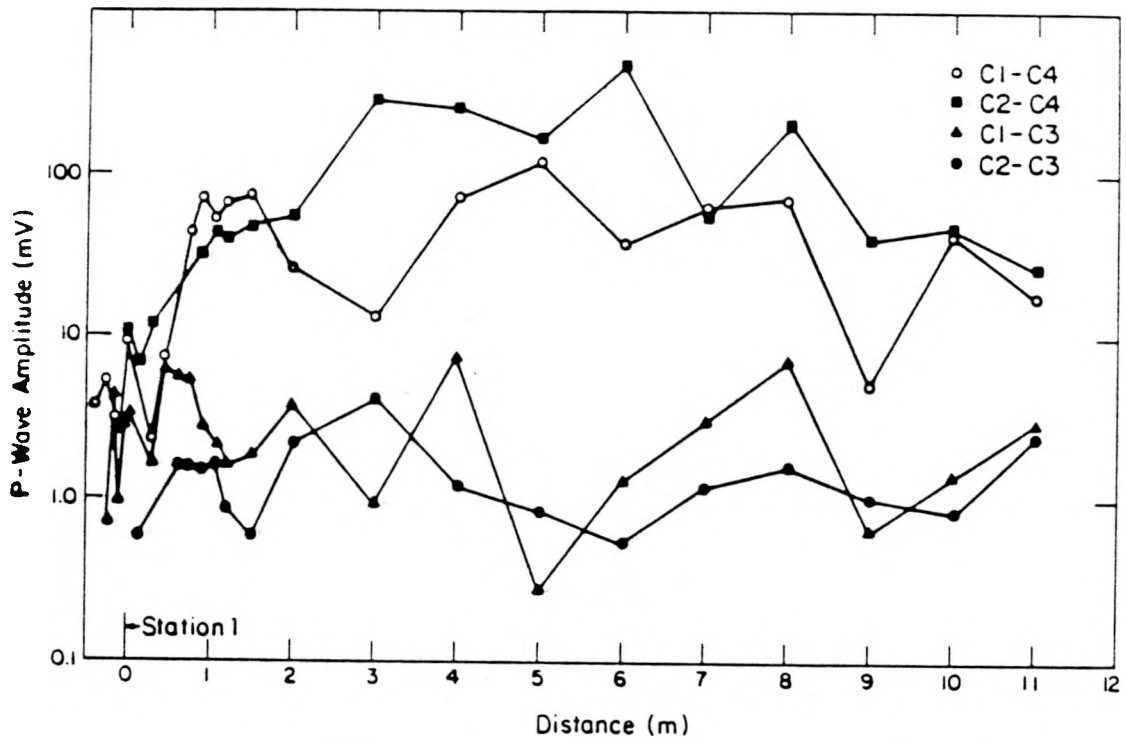

Figure 2.18 First arrival amplitudes for the four diagonal travel paths.

The first arrival amplitudes for the three vertical boreholes average 0.85 mV (±0.83). This is lower than any of the averages for the four horizontal boreholes. These data are consistent with other data collected in these three boreholes, and indicates the rock below the Heater Test

room floor has a greater fracture density than the rock adjacent to the West Access tunnel.

2.9. Relative Q

A relative rock quality (Q) analysis was performed to obtain another measurement of the signal attenuation properties of the basalt. This analysis takes into account frequency as well as amplitude. The technique used to determine the relative Q values is based on techniques used by Johnston and Toksöz (1980) for laboratory cores and by Majer and McEvilly for field data (1978).

The Fourier amplitude for a plane seismic wave traveling in an isotropic media can be expressed by the following equation:

$$A(f) = G(x)e^{-\alpha(f)}e^{i(2\pi ft - kx)} \tag{2.4}$$

A = *Fourier Amplitude*

f = *frequency*

x = *distance*

k = *wave number*

v = *velocity*

G = *geometric factor*

$\alpha(f)$ = *attenuation coefficient*

It is assumed that $\alpha(f)$ is a linear function of frequency and that it can be expressed as:

$$\alpha(f) = \frac{\pi f T}{Q} \tag{2.5}$$

T= travel time

Q= Rock Quality Factor

To obtain the relative Q values for the basalt in situ, a ratio is taken of the magnitudes of two complex wave equations, one equation expressing the Fourier amplitude for the wave of interest and another expressing the Fourier amplitude of a reference wave:

$$\frac{A_s(f)}{A_r(f)} = \frac{G_s(x)}{G_r(x)} e^{\alpha_r - \alpha_s} \tag{2.6a}$$

For $G_s(x) = G_r(x)$,

$$A_s(f) = A_r(f) e^{\alpha_r - \alpha_s} \tag{2.6b}$$

$$\ln \frac{A_s(f)}{A_r(f)} = \alpha_r - \alpha_s \tag{2.7}$$

Cancelling the geometric factor in equations 2.6b and 2.7 is done to simplify the equations. This will not cause any error in the Q values for the vertical and horizontal travel paths, where the distances between the boreholes are approximately equal. Assuming the geometric factors are equal to 1/x, cancelling them from equations 2.6b and 2.7 will increase the Q values for the diagonal paths by approximately 10%. To apply equation 2.7, a standard Fast Fourier Transform (FFT) was performed on all

the P-waves. The spectrum with the greatest amplitudes at and around 30 kHz was then found and used for the reference Fourier spectrum. This made $A_r(f)$ always greater than $A_s(f)$, and α_r always less than α_s (equation 2.6b). The Fourier amplitude spectrum of the P-wave measured between boreholes C1 and C2 at station 18 was found to contain the greatest amplitudes around 30 kHz, and therefore it was used for the reference spectum. An arbitrary Q value of 100 was assigned to this spectrum, and by applying equation 2.7, relative Q values could be obtained from the other spectra. Table A.2 lists the relative Q values, calculated at frequencies centered about 30 kHz, for each pair of boreholes at each station.

Figures 2.19 and 2.20 illustrate the relative Q values for the various travel paths. Figure 2.19 shows the relative Q values for the vertical and horizontal travel paths. The Q values for the vertical travel paths are approximately five times greater than those obtained for the horizontal travel paths. Again, the more joints the waves travel through the more attenuated they become. Therefore, P-waves traveling through the vertical travel paths appear to intersect fewer joints than P-waves traveling through the horizontal travel paths.

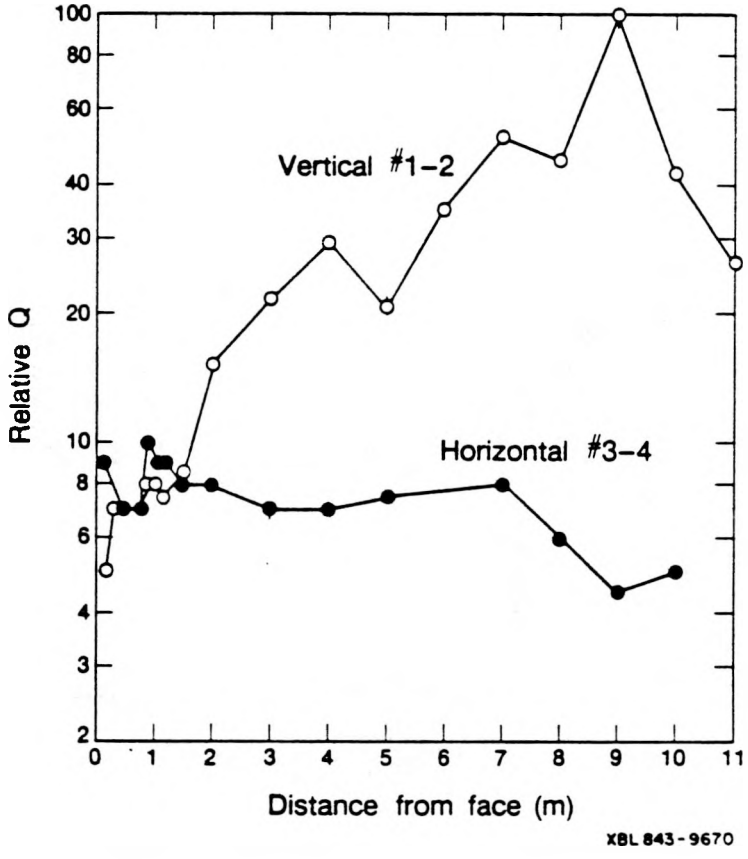

Figure 2.19 Relative Q values for the vertical and horizontal travel paths.

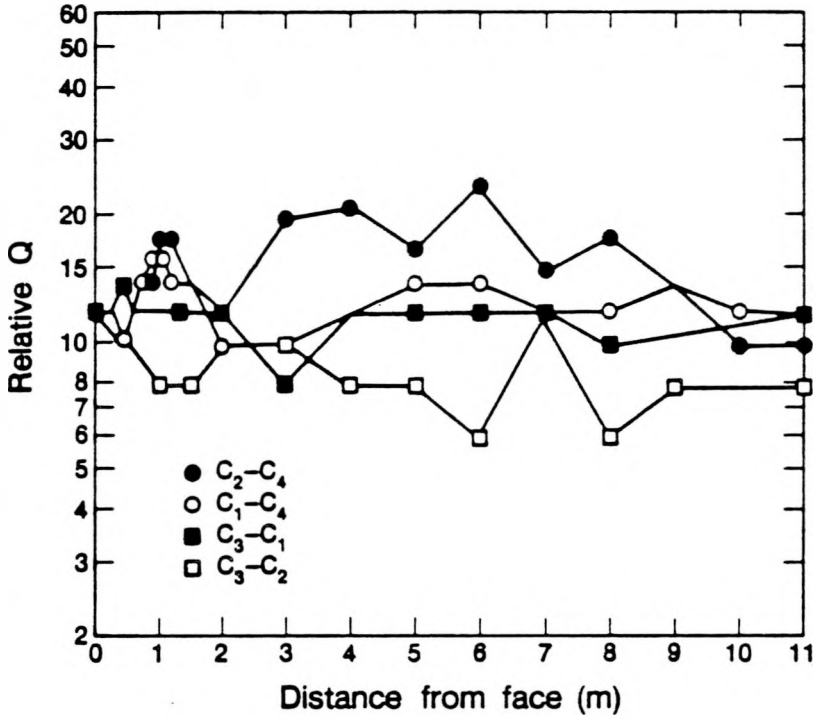

Figure 2.20 Relative Q values for the four diagonal travel paths.

Figure 2.20 illustrates the relative Q values for the four diagonal travel path orientations. Table 2.7 lists the average Q values of the last 11 stations for each of the diagonal borehole pairs. This table shows that the average Q value measured between boreholes C2 and C4 is the greatest and between C3 and C2, the least. It again appears the rock between boreholes C3 and C2 has a higher fracture density than the rock

between C2 and C4.

Table 2.7
Average relative Q values for the last 11 stations for the diagonal travel paths.

Borehole Pair	Q value	
C2-C4	8.2	± 1.9
C1-C4	6.2	± 1.2
C3-C1	5.1	± 0.9
C3-C2	4.3	± 0.7

Only the relative Q values measured in the vertical travel paths between boreholes C1 and C2 show a decline in magnitude as the borehole collar is approached. This may be due to the fact that the Fourier amplitudes measured for the other travel path orientations are about 1/30 of the Fourier amplitudes measured in the vertical direction. The further attenuation that occurs near the borehole collars may have been masked by this initial difference. The uneven stresses which occurred in the oversized sections of the boreholes may also have affected the data.

The relative Q values for the three vertical boreholes are listed in Table A.3. The average relative Q value of these boreholes is 8.7 (±2.0). The greater density in jointing in the Heater Test room floor, as indicated by the data thus far presented, is expected to have attenuated the signals to a greater degree. The reason the average Q value is greater than expected may be because the geometric factors were cancelled from equation 2.7. The distance between boreholes 2M12 and 2M7 is only 2/3 the distance between the horizontal boreholes. Therefore, the P-waves are less attenuated than if they had traveled through 3.0 m of rock.

The conclusions based on the relative Q values are essentially the same as those obtained from the first arrival amplitudes. The main

difference between the two techniques is that the first arrival method looks at the amplitude of the first arriving wavelet without regard to frequency, while the relative Q technique looks at Fourier amplitudes centered about a specific frequency, 30 kHz for this study. If the frequency of the first arriving wavelet is in the range where the Q values are assumed to be frequency independent, as the data in this study indicated, the two techniques should yield the same results. The advantage to the first arrival technique is that it can be done quickly without the aid of a digital computer. The advantage of the relative Q technique is that it is more universally used and can be applied with greater consistency. Also a quantitative value for Q can be obtained in the eithor the field or laboratory.

3. Laboratory Testing.

3.1. Introduction

The purpose of the laboratory measurements was to augment the results of the field testing by providing geomechanical values for the intact version of the Pomona entablature. When compared with the laboratory results, the field values should be consistent with a more jointed version of the same rock.

A schematic diagram of the equipment used for the laboratory testing is illustated in Figure 3.1. This system is essentially the same as a system used to measure the static and dynamic elastic properties of rocks from the Canadian Shield (King, 1983). The main components of the system are:

- Digital Oscilloscope.
- P- and S-wave transducers.
- Power source and pulse trigger.
- Selectable gain amplifier.
- Hydraulic press.

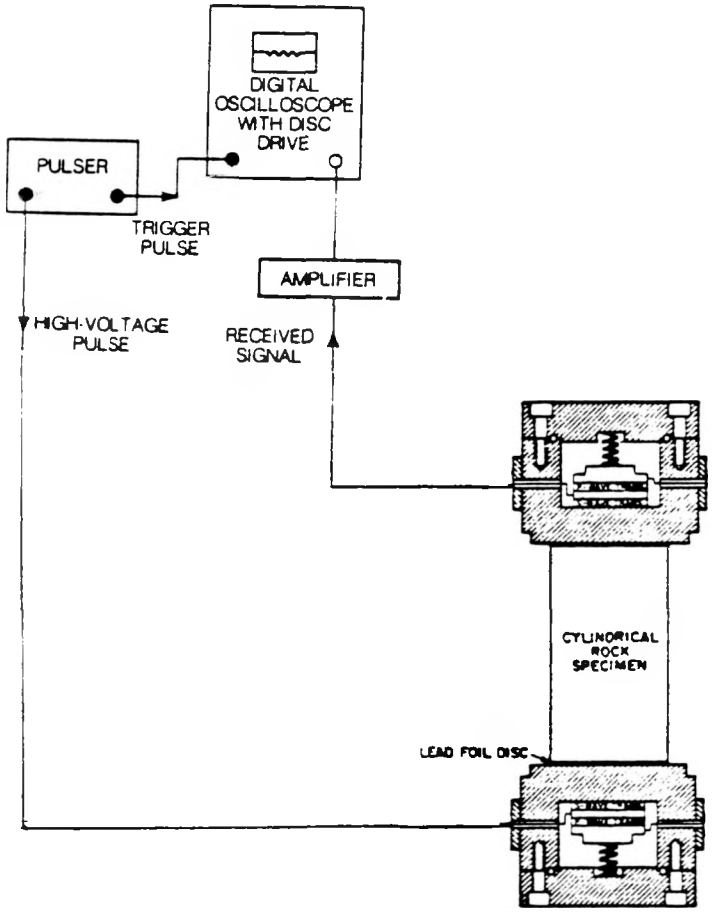

Figure 3.1 Schematic diagram of laboratory test equipment.

The P-wave and S-wave piezoelectric crystals are mounted in the form of a sandwich inside the transducers. This enables both P- and S-wave measurements to be made without disturbing the rock specimen. The Fourier amplitudes for the P- and S-waves emitted from the

transducers peak at approximately 500 kHz, and the S-wave poling is across two half disks.

3.2. Measurement Procedure

Laboratory testing was performed on ten cores retrieved from the four horizontal boreholes in the west wall of the West Access tunnel. Two cores were retrieved from borehole C1, three from C2, three from C3, and two from C4. The finished core specimens averaged 50 mm in length and 44 mm in diameter. The specimens were tested both dry and saturated. The specimens were dried by placing them in a vacuum oven for 48 hours at 105 °C. To saturate the specimens, they were first placed in a vacuum for 72 hours. They were then immersed in de-aired de-ionized water while the vacuum was maintained. They remained immersed in the water at atmospheric pressure for four days before testing.

Once prepared in their dried or saturated state, the core specimens were ready for testing. The test procedure began with placing a disk of lead foil at either end of a specimen, and then placing the specimen plus foil between the transducers. The lead foil is used to improve acoustic coupling between the basalt specimen and the aluminum body of the transducers. This assembly was then placed between the platens of the hydraulic press. Loads of 1.0, 2.0, and 3.0 metric tons were applied during testing. This resulted in axial stresses of approximately 7, 14, and 21 MPa between the transducers and the core specimens.

With the specimens in place and the load applied, a series of repetitive electric pulses were applied to one of the two transmitting piezoelectric crystals and the oscilloscope simultaniously. The piezoeletric

crystal in turn propagated a series of repetitive seismic wavetrains through the core which were sensed by the corresponding piezoelectric crystal in the receiving transducer and transmitted to the oscilloscope.

Upon receiving the synchronous timing pulse, the oscilloscope began a sweep, sampling every 50 ns for 102 μs. Typically the P- and S-wavetrains arrived after delays of 16 and 25 μs respectively. Individual traces could be stored temporarily on the CRT of the oscilloscope. As with the field data, the portion of the trace prior to the P- or S-waves arrival was examined until a signal is found which exhibited the lowest attainable amount of background noise. This signal was then stored on a floppy disk. Approximately ten signals were examined for every one saved. This process was then repeated with the other piezoelectric crystal. When both a P- and an S-wave were saved, a new measurement was made with either a new load and/or a new specimen. Following this procedure, all ten core specimens were sampled both dry and saturated.

3.3. Laboratory Velocity Determination

The velocities for the specimens were determined in the same manner as the velocities for the field data. The amplitudes of the first arriving wavelets for both the P- and S- waves were many times greater than the background noise, making picking of the first arrivals an easy matter. The time the signal spent traveling in the lead foil and transducers was found by placing two pieces of lead foil between the transducers and measuring the first arrival time for both the P- and S-waves. The delay times were found to be 6.85 and 10.85 μs for the P- and S-waves respectively. The delay times were subtracted from the first arrival times and equation 2.1 was used to calculate the velocities.

The specimen velocities and their relation to saturation, and to the boreholes from which they were retrieved, are listed in table A.4. The average S-wave velocity for all the specimens remained approximately constent when they were saturated and axial stress was increased. Their average S-wave velocity at 7 MPa, 3357 m/s, is 69 m/s greater than the average S-wave velocity for the vertical travel paths between boreholes C1 and C2. The average P-wave velocity for all the specimens increased with both increased saturation and increased axial stress. The greatest P-wave velocity found in the specimens, 6020 m/s, is 272 m/s slower than the greatest P-wave velocity found in the field. The greatest P-wave velocity in the field was found in a vertical travel path at station 15. Visual inspection and the tendency for the velocities to increase with increasing axial stress indicates the presence of hairline and microfractures within the specimens. The laboratory and field data appear to indicate there is an anisotropy in the density of hairline and microfracturing between the horizontal and vertical travel paths. The axes of the cores are perpendicular to the vertical planes used to define the stations used in the field. It appears that the waves traveling through the cores intersect more hairline cracks and microfractures than the waves traveling along the vertical travel paths in the field. There may possibly be flow structure within the basalt that is not visable, without the use of thin sections, that is also causing variations in velocities between horizontal and vertical travel paths. The higher frequencies used in the laboratory studies may also make the laboratory P-wave velocities more sensitive to these small fractures. The wavelengths of the laboratory and field P-waves are approximately 1.2 and 20 cm respectively. The hairline and microfractures may have a greater retarding affect on the laboratory P-waves because of

these waves' smaller wavelengths. Vertically oriented core samples need to be tested to verify the last two assumptions.

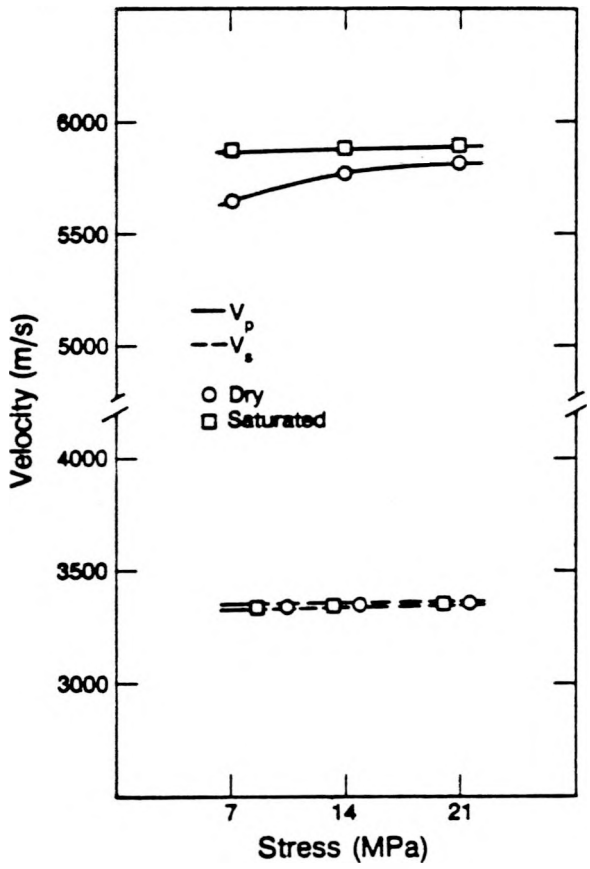

Figure 3.2 The average P- and S-wave velocities for the dry and saturated cores.

Velocities measured along diagonal travel paths between two of the horizontal boreholes are greater than the dried core velocities and less than the saturated core velocities. These data and presence of standing water in one of the boreholes are taken to indicate that most of the basalt tested in the field was probably nearly saturated at the time of the cross-hole tests.

The P- and S-wave velocities found along paths between the three vertical boreholes are from 2000 to 4000, and 1500 to 2500 m/s slower than the P- and S-wave velocities found for the laboratory specimens respectively. Again it appears that the basalt below the Heater Test room is highly fractured.

Whether drying of the rock around the heater during the thermal cycle or drying of the rock directly adjacent the West Access tunnel from being exposed to a free surface, contributed to the lowering of velocities in these areas is difficult to ascertain. Experiments have shown that rock specimens can become saturated, by the absorption of water vapor through capillary action of microfractures, without coming into contact with free standing water (King, 1984). The jointing in the West Access tunnel enabled water to percolate through the rock mass there, and free standing water was found in borehole C4. The presence of this water would enable moisture to be absorbed and retained in the small openings of the rock. Also, Poisson's ratio appeared to go up with increased jointing found in the diagonal travel paths between boreholes C3 and C2, which according to O'Connell and Budiansky (1977), indicates a saturated rock. Therefore, it seems unlikely that the rock adjacent to the West Access tunnel was dry. On the other hand, the Heater Room opening might have prevented water from percolating through the rock below. For this area of rock to become saturated, water would need to be drawn into it from the surrounding rock mass. The data in these tests indicate that this area of rock was highly fractured. The increased permeability due to the increased fracturing may have minimized the absorption of water into the rock mass directly below the Heater Test room. Poisson's ratio was also found to be the lowest in travel paths closest to the heater.

Therefore, it is possible that the basalt below the Heater Test room remained dry after the thermal cycle and this dry state contributed to the low P- and S-wave velocities found there.

3.4. Laboratory Dynamic Moduli

Young's moduli and Poisson's ratios were calculated from the specimen P- and S-wave velocities, using equations 2.2 and 2.3. They are listed in Table A.4. Figure 3.3 illustrates the relationship between averages of Young's modulus and Poisson's ratio, and saturation and load. Young's modulus was found to increase with both increased saturation and increased axial stress. The greatest values of Young's Modulus determined from the laboratory P- and S-wave velocities are less than the greatest Young's modulus found between boreholes C1 and C2. Equation 2.4 shows that Young's modulus is more sensitive to changes in the P-wave velocity than to changes in the S-wave velocity. Therefore, the factors which cause greater P-wave velocities in the vertical travel paths probably also cause the greater Young's moduli. Poisson's ratio primarily increased with saturation. Poisson's ratio as calculated from equation 2.3 is a function of V_p/V_s. As the P-wave velocity increased with saturation and the S-wave velocity remained constent, Poisson's ratio also increased. The increase in the P-wave velocity due to increased stress caused a small increase in the values of Poisson's ratios obtained from the dry specimens, and no discernable increase in Poisson's ratio obtained from the saturated specimens. The Poisson's ratios measured in the laboratory specimens are 10 to 30% lower than the Poisson's ratios found in the field. Because an increase in jointing in a saturated rock will cause Poisson's ratio to increase, these data indicate the basalt in the field is probably much more jointed than the cores.

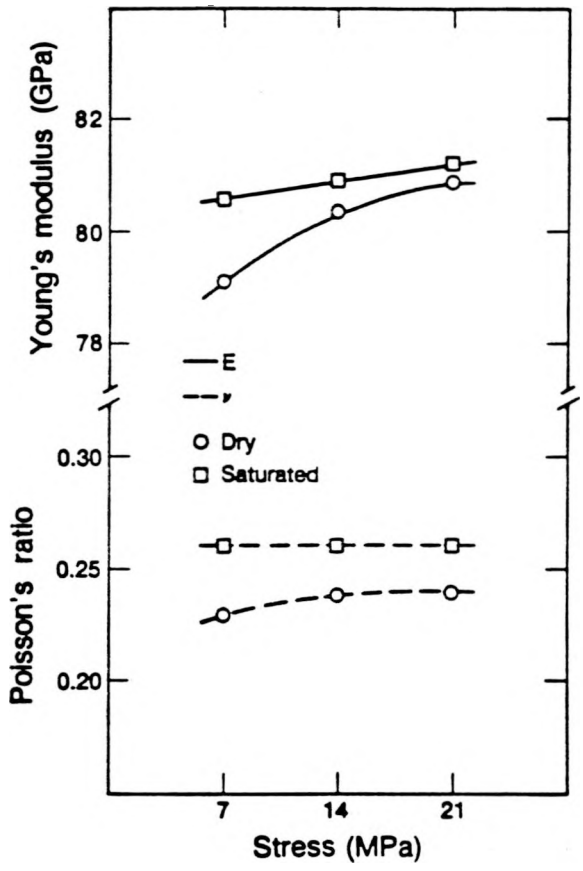

Figure 3.3 Average Young's moduli and Poisson's ratios for the dry and saturated cores.

3.5. Rock Quality Factor (Q)

The Q analysis performed on the core data in the laboratory was essentially the same as the Q analysis performed on the field data. The only difference was that the Q of the reference Fourier amplitude spectum was known, rather than arbitrarily assigned as in the case of the field data. To obtain the reference spectrum, an aluminum block with a known Q value and the same dimensions as the laboratory specimens was prepared and tested. The Fourier amplitude spectra obtained from the P- and S-waves propagated through the aluminum sample were than used for the references. Unlike the field data, mode converted P-waves did not

interfere appreciably with the first arrivals of the S-wave signals, and therefore Q values were obtained for both the P-and S-waves. The ten laboratory specimens were tested both dry and saturated using an axial load of 1.0 metric ton, which corresponded to an axial stress of approximately 7 MPa. Three specimens were further tested using axial loads of 1.0, 2.0, and 3.0 metric tons.

The Q values obtained from the specimens are listed in Table A.4. The Q values obtained for the S-waves were greater than the Q values obtained for the P-waves, and both sets of values increased with both saturation and load (Figure 3.4). Q values obtained in a previous study (Johnston and Toksöz, 1980) also tended to increase with increased axial stress, but these Q values decreased with saturation. For the Johnston and Toksöz experiment a porous sandstone and limestone were studied. Their porosities were due to intergranular openings. On the other hand, the porosity in the Pomona basalt cores was due to hairline cracks and microfracturing. The openings in the basalt had much lower aspect ratios. O'Connell and Budiansky (1977) argue that seismic attenuation is caused in part by the presence of fluids within the pore space of the rock. They describe three types of flow behavior within a rock in response to a seismic wave; dry, isobaric, and saturated isolated. A rock with interconnected porosity exhibits dry behavior when fluids can move freely within the pore spaces of the rock, due to seismic induced deformations of the rock matrix. No pressure gradients are induced in the fluids and the rock behaves as if dry. A rock exhibits isobaric behavior when fluids can flow between cracks but no bulk movement of fluid occurs. In this case, as some cracks are compressed others open and the fluids flow in between. The sandstone and limestone samples that

were tested by Johnston and Toksöz (1980) appeared to exhibit this kind of behavior. The last type of behavior, saturated isolated, occurs when fluids do not flow between cracks. Because of the smaller aspect ratios and the lower permeability of the Pomona basalt, fluids would not be expected to flow as freely between cracks as they could in the sandstone or limestone. Therefore, the Pomona basalt would exhibit behavior more approaching type three than either the sandstone or limestone. As the behavior of the rock changes from type two to type three, the rock begins to behave more like a solid, and the attenuation is reduced. This is probably why the Pomona basalt Q values increased with saturation while the sandstone and limestone Q values decreased with saturation. It appears that the saturated Q values are sensitive to crack aspect ratios, decreasing with saturation when aspect ratios are near one and increasing with saturation when aspect ratios are much less than one.

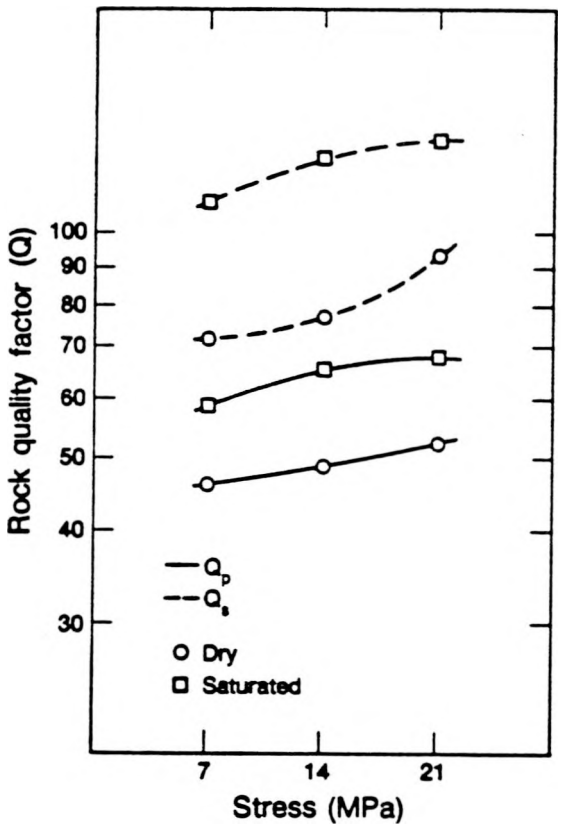

Figure 3.4 Average Q values for the dry and saturated cores.

The laboratory data indicates that the value of 100 assigned to the field Fourier amplitude reference signal was probably too high. The rock properties measured in the laboratory specimens always indicated a slightly less competent rock than the rock properties measured in the vertical travel paths[1]. However, the difference between these two sets of values was always small. It was assumed that the Q values would also follow this trend. The average Q value of 50 for the saturated laboratory specimens would be expected to be fairly close to the absolute Q value

[1] Whether the laboratory specimens are actually less competent than the rock along the vertical travel paths in the field was not conclusively established. The reader is refered to the discussion given in the section on laboratory velocity determinations.

for the vertical travel paths between boreholes C1 and C2 where the reference signal was recorded. Because the exponent in equation 2.5 must remain the same regardless of the Q value assigned to the reference signal, this exponent may be used to adjust the relative in situ Q values to reflect the true absolute in situ Q values of the rock more accurately. This avoids having to recalculate the new Q values from the original spectra. The expression used to make these adjustments is simply:

$$\frac{T_r}{Q_r} - \frac{T_s}{Q_s} = \frac{T_r}{Q_r} - \frac{T_s}{Q_s}$$

relative values *absolute values*

Table 3.1 lists the borehole pairs, their average relative Q values, their new average Q values, and the percentage difference between the two. The error between the two sets of Q values for all but the vertical travel paths was less than 12%. It can safely be assumed that the new values are probably within 5% of the true absolute in situ Q values for the basalt.

Table 3.1
Relative Q adjustments.

Borehole pair	Old Q	Adjusted Q	% change
C1-C2	39.0	23.4	40
C3-C4	6.7	6.4	5
C2-C4	8.2	7.3	11
C1-C4	6.2	5.7	8
C1-C3	5.4	5.1	6
C3-C2	4.3	4.1	5

3.6. Rock Quality Designation

The rock quality designation (RQD) was provided by Rockwell International for the four horizontal boreholes in the West Access tunnel (Figure 3.5). The RQD values are measurements of the density of fractures found in the cores. A 30 cm segment of core is examined for fractures. All the lengths of unfractured core over 10 cm long within this segment are added together and divided by 30 cm to obtain the RQD values. They are a measure of the jointing found in the boreholes. The cores retrieved from boreholes C1 and C4 are less jointed than the cores retrieved from borehole C3: borehole C2 has the greatest number of joints. Because the jointing in the cores reflect the jointing in the rock, the RQD values indicate the rock in the vicinity of boreholes C1 and C4 is less jointed than the rock in the vicinity of C3 and C2. It was assumed that care was taken to insure that fractures caused by the coring process were not counted as joints. The data measured along the diagonal travel paths and the RQD values indicate the density of jointing is greatest in the bottom left side of the diamond formed by the four boreholes and least in the bottom right side of the diamond (Figure 3.6).

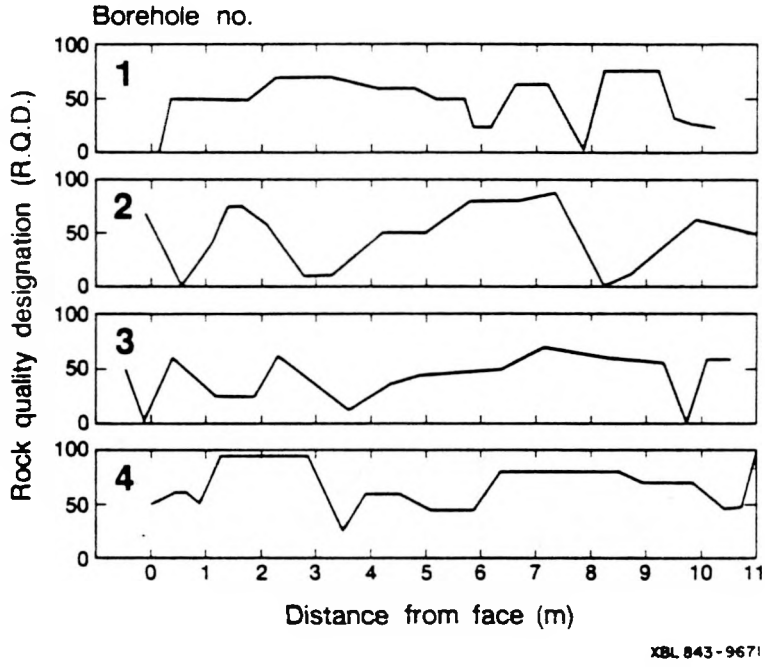

Figure 3.5 Rock quality designation for the four horizontal boreholes.

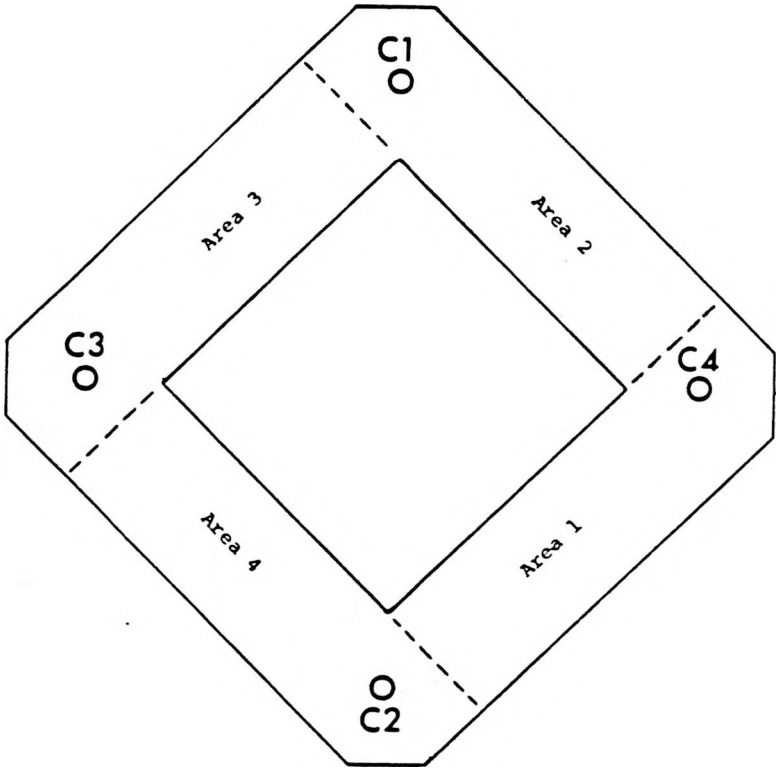

Figure 3.6 The fracture density determined from the seismic and RQD data. Area 1 was the lowest density of columnar and discontinuous cross-jointing. The density of jointing increases counterclockwise around the diamond.

4. Conclusion

The data collected in the field and laboratory, and the RQD values provided by Rockwell International, indicate the fracture density within the basalt is anisotropic and inhomogeneous. The data indicate that waves traveling in the horizontal direction encounter a greater fracture density than waves traveling in the vertical direction. This anisotropy is consistent with the columnar characteristics of the Pomona entablature. The laboratory data, when compared to the field data, indicate the density of the smaller less obvious hairline cracks and microfractures is also anisotropic. It appears that a greater density of these smaller fractures are encountered by waves traveling through the horizontally oriented core specimens than encountered by waves traveling along the vertical travel paths in the field. The matrix of the basalt may also be anisotropic with respect to seismic wave propagation, however thin sections would need to be examined to verify this. The data also indicate the density of both the columnar and low-angle discontinuous cross-jointing is inhomogenious. The density of the columnar and cross-jointing is lowest in the bottom right quadrant of the of the diamond formed by the four boreholes and increases in a counterclockwise direction around the diamond. The data indicate the rock damage due to the blasting used in mining the tunnel is confined to the first 1.5 m of rock adjacent to the tunnel side. The data indicate the rock adjacent to the West Access tunel was probably saturated during the time the cross-hole tests were made.

The data taken in the floor of the Heater Test room indicate the basalt there is more fractured than the basalt adjacent to the West Access tunnel. When compared to data collected in this area prior to the thermal cycle experiments, these data show the rock is currently more

fractured than in the past, presumably as a result of the heating cycle. Finally, it appears the rock in the floor of the Heater Test room had been dried during the heating cycle and had remained so when the field tests were performed.

5. Bibliography

Duvall, W. I., Miller, R. J., and Wang, F. D.. "Preliminary Report on Thermal Properties of Basalt; Drill Hole DC-10; Pomona Flow- Gable Mountain," RHO-BWI-LD-5, Rockwell Hanford Operations, Richland, Washington, (1978).

Hadley, Kate. "Comparison of Calculated and Observed Crack Densities and Seismic Velocities in Westerly Granite," *Journal of Geophysical Research*, 81, 3484-3494, (July 1976).

Jeager, J. C. and Cook, N. G. W.. *Fundamentals of Rock Mechanics* (New Yok John Wiley and Sons, 1976).

Johnston, D. H. and Toksöz, M. N.. "Ultrasonic P- and S-Wave Attenuation in Dry and Saturated Rocks Under Pressure," *Journal of Geophysical Research*, 85, 925-936, (1980).

King, M. S.. "Wave Velocities in Rocks as a Function of Changes in Overburden Pressure and Pour Fluid Saturants," *Geophysics*, 31, 50-73, (1966).

King, M.S.. "Static and Dynamic Elastic Properties of Rocks from the Canadian Shield," *Journal of Rock Mechanics* and *Mining Sciences* and *Geomechanical Abstracts*, 20, 237-241, (1983).

King, M. S.. "Elastic Wave Velocities in Quartz Monzonite at Different Levels of Water Saturation," *International Journal of Rock Mechanics* and *Mining Sciences* and *Geomechanical Abstracts*, 21, (1984).

Majer, E. L. and McEvilly, T. V.. "Seismological Investigations at the Geysers Geothermal Field," *Geophysics*, 44, 246-269, (February 1979).

Moak, D. J. and Wintczack, T. M.. "Near-Surface Test Facility Phase I Geologic Site Report," RHO-BWI-ST-8, Rockwell Hanford Operations, Richland, Washington, (1980).

O'Connell, R. J. and Budiansky, B.. "Visco-Elastic Properties of Fluid-Saturated Cracked Solids," *Journal of Geophysical Research*, 82, 5719-5735, (December 1977).

Paulsson, B. N. P. and King, M. S.. "Between-Hole Acoustic Surveying and Monitoring of a Granitic Rock Mass," *International Journal of Rock Mechanics* and *Mining Sciences* and *Geomechanical Abstracts*, 17, 371-376, (December 1977).

Schmidt, B., Daly, W.F., Bradley, S.W., Squire, P. R., and Hulstrom, L. D.. "Thermal and Mechanical Properties of Hanford Basalts: Compilation and Analysis," RHO-BWI-C-90, Rockwell Hanford Operations, Richland, Washington, (1980).

Appendix A

Table A.1

Crosshole Test Measurement Positions

Station No.	Distance From Hole Collar (m)						
	Borehole No.						
	C1	C2	C3	C4	2M7	2M9	2M12
1	0.756	0	0.536	0.235	3.000	3.006	3.018
2	0.906	0.15	0.686	0.385	4.250	4.256	4.268
3	1.056	0.30	0.836	0.535			
4	1.206	0.45	0.986	0.685			
5	1.356	0.60	1.136	0.835			
6	1.506	0.75	1.286	0.985			
7	1.656	0.90	1.136	1.135			
8	1.806	1.05	1.586	1.285			
9	1.956	1.20	1.736	1.435			
10	2.256	1.50	2.036	1.735			
11	2.756	2.00	2.536	2.235			
12	3.756	3.00	3.536	3.235			
13	4.756	4.00	4.536	4.235			
14	5.756	5.00	5.536	5.235			
15	6.756	6.00	6.536	6.235			
16	7.756	7.00	7.536	7.235			
17	8.756	8.00	8.536	8.235			
18	9.756	9.00	9.536	9.235			
19	10.756	10.00	10.536	10.235			
20	11.756	11.00	11.536	11.235			

Table A.2

Crosshole Seismic Test Results

Transmitter Hole No. C2 Receiver Hole No. C1

Measurement No.	Station No.	Travel Distance (m)	Travel Time (μsec) P-wave	Travel Time (μsec) S-wave	Velocity m/sec P-wave	Velocity m/sec S-wave	Poisson's Ratio ν	Young's Modulus E (MPa)	Wave Amp. P-wave (mV)	Relative Q
66-69	20	2.949	520	953	5898	3216	0.289	75.9	661	26.0
70-73	19	2.944	517	967	5924	3162	0.301	74.1	736	43.0
74-77	18	2.938	498	920	6146	3324	0.293	81.4	1466	100.0
78-81	17	2.932	497	941	6151	3242	0.308	78.3	742	46.0
82-85	16	2.932	486	903	6292	3382	0.297	84.5	790	52.0
86-89	15	2.929	486	900	6285	3390	0.295	84.8	734	35.5
90-93	14	2.923	488	903	6246	3371	0.294	83.8	310	21.0
94-97	13	2.920	486	919	6266	3307	0.307	81.4	505	29.5
98-101	12	2.918	487	902	6248	3370	0.295	83.8	372	22.0
102-105	11	2.916	492	931	6178	3258	0.307	79.1	337	20.0
106-108*	10	2.915	523	963	5795	3145	0.291	72.7	79.4	8.5
109-113	9	2.914	522	986	5805	3067	0.306	70.0	43.2	7.5
113-116	8	2.914	530	958	5714	3161	0.280	72.8	24.8	8.0
117-120	7	2.914	522	943	5805	3213	0.279	75.2	123	8.0
121-124	6	2.914	530	937	5714	3234	0.264	75.3	28.8	7.0

* Duplicate Nos. assigned to two records.

Table A.2

Crosshole Seismic Test Results

Transmitter Hole No. C2 **Receiver Hole No.** C1

Measurement No.	Station No.	Travel Distance (m)	Travel Time (μsec) P-wave	Travel Time (μsec) S-wave	Velocity m/sec P-wave	Velocity m/sec S-wave	Poisson's Ratio ν	Young's Modulus E (MPa)	Wave Amp. P-wave (mV)	Relative Q
153-156	5	2.907	527	975	5734	3096	0.294	70.7	1.13	
149-152	3	2.907	556	1073	5424	2803	0.318	59.0	2.16	6.0
125-128	2	2.900	521		5566				5.5	5.0
299-302	S5	2.995	961	1690	3183	1811	0.261	23.6	1.56	
303-306	S4	2.962	793	1640	3832	1847	0.349	26.2	8.5	
307-310	S3	2.936	668	1161	4531	2610	0.252	48.6	8.2	
311-314	S2	2.917	607	1128	4969	2671	0.297	52.7	14.8	
315-318	S1	2.905	572	1057	5263	2845	0.294	59.6	18.8	
				Repeat Measurements						
319-322	3	2.907	540	1071	5590	2809	0.331	59.8	46.6	8.0
323-326	7	2.914	537	1020	5636	2961	0.309	65.4	50.6	8.0
327-330	8	2.914	529	1002	5125	3017	0.308	67.8	51.2	8.0
331-334	11	2.916	520	962	5832	3149	0.294	73.1	121.7	12.0
335-338	13	2.920	513	911	5923	3337	0.268	80.4	520	22.0

Table A.2

Crosshole Seismic Test Results

Transmitter Hole No. C3 Receiver Hole No. C4

Measurement No.	Station No.	Travel Distance (m)	Travel Time (μsec) P-wave	Travel Time (μsec) S-wave	Velocity m/sec P-wave	Velocity m/sec S-wave	Poisson's Ratio ν	Young's Modulus E (MPa)	Wave Amp. P-wave (mV)	Relative Q
1-4	20	3.069	599	1077	5301	2948	0.276	63.2	145	
5-8	19	3.056	622	1095	5076	2886	0.261	59.8	170	5.0
9-12	18	3.042	643	1278	4883	2449	0.332	45.5	22	4.5
13-16	17	3.029	548	1106	5737	2831	0.339	61.1	115	6.0
17-20	16	3.011	611	1215	5095	2554	0.332	49.5	146	8.0
21-24	15	2.996	617	1160	5018	2665	0.304	52.8	19	
343-346	14	2.984	653	1250	4714	2458	0.313	45.2	1.52	7.5
347-350	13	2.964	646	1235	4735	2472	0.313	45.7	2.04	7.0
351-354	12	2.959	604	1232	5067	2474	0.344	46.8	1.42	7.0
355-358	11	2.946	622	1195	4894	2542	0.315	48.4	4.4	8.0
359-362	10	2.939	727	1364	4157	2213	0.302	36.3	.96	8.0
363-366	9	2.936	723	1331	4176	2267	0.291	37.8	.82	9.0
367-370	8	2.932	693	1430	4357	2103	0.348	34.0	.16	9.0
371-374	7	2.929	730	1485	4127	2022	0.342	31.3	1.6	12.5
375-378	6	2.929	729	1520	4131	1974	0.352	30.0	2.36	7.0

Table A.2

Crosshole Seismic Test Results

Transmitter Hole No. C3 Receiver Hole No. C4

Measurement No.	Station No.	Travel Distance (m)	Travel Time (μsec) P-wave	Travel Time (μsec) S-wave	Velocity m/sec P-wave	Velocity m/sec S-wave	Poisson's Ratio ν	Young's Modulus E (MPa)	Wave Amp. P-wave (mV)	Relative Q
379-381	4	2.914	721	1518	4157	1966	0.356	29.9	2.5	7.0
525-528	2	2.913	880	1682	3387	1770	0.312	23.4	.68	9.0
529-532	S1	2.913	910	1874	3273	1585	0.347	19.3	.88	9.0

Table A.2

Crosshole Seismic Test Results

Transmitter Hole No. C2 Receiver Hole No. C4

Measurement No.	Station No.	Travel Distance (m)	Travel Time (μsec) P-wave	Travel Time (μsec) S-wave	Velocity m/sec P-wave	Velocity m/sec S-wave	Poisson's Ratio ν	Young's Modulus E (MPa)	Wave Amp. P-wave (mV)	Relative Q
443-446	20	2.059	388	705	5595	3078	0.283	69.2	27.2	5.0
447-450	19	2.050	394	719	5481	3001	0.286	66.0	48	5.0
451-454	18	2.047	386	695	5593	3106	0.277	70.2	40	7.0
455-458	17	2.041	374	671	5766	3214	0.275	75.0	208	10.0
459-462	16	2.036	371	663	5801	3247	0.272	76.4	56.6	7.0
463-455	15	2.033	365	653	5893	3295	0.273	78.7	476	14.0
467-470	14	2.034	370	688	5811	3120	0.298	71.9	117	8.0
471-474	13	2.034	368	679	5845	3163	0.293	73.7	252	12.0
475-478	12	2.035	371	673	5798	3195	0.282	74.5	290	11.0
479-482	11	2.035	381	690	5637	3112	0.281	70.6	56.4	6.0
483-486	10	2.038	388	742	5538	2887	0.314	62.3	49.2	7.0
487-490	9	2.035	408	734	5245	2915	0.276	61.8	40	9.0
491-494	8	2.035	411	743	5205	2878	0.280	60.4	44	9.0
495-498	7	2.035	406	749	5273	2854	0.293	60.0	33.6	7.0
541-544	3	2.025	578	1046	3629	2005	0.280	29.3	12	

Table A.2

Crosshole Seismic Test Results

Transmitter Hole No. C2 Receiver Hole No. C4

Measurement No.	Station No.	Travel Distance (m)	Travel Time (μsec) P-wave	Travel Time (μsec) S-wave	Velocity m/sec P-wave	Velocity m/sec S-wave	Poisson's Ratio ν	Young's Modulus E (MPa)	Wave Amp. P-wave (mV)	Relative Q
545-548	2	2.027	583	1108	3600	1891	0.310	26.7	6.8	
549-552	S1	2.030	585	1185	3593	1767	0.341	23.8	11.6	
				Repeat Measurements						
615-616	12	2.035	368	670	5848	3210	0.284	75.4	294	
613-614	13	2.034	367	672	5862	3198	0.288	75.0	179	9.0
603-604	14	2.034	367	659	5862	3265	0.275	77.4	165	9.0
593-594	15	2.033	364	667	5910	3222	0.289	76.2	104.8	9.0
583-594	16	2.036	364	669	5919	3216	0.290	76.0	10.0	9.0

Table A.2

Crosshole Seismic Test Results

Transmitter Hole No. C4 Receiver Hole No. C1

Measurement No.	Station No.	Travel Distance (m)	Travel Time (μsec) P-wave	Travel Time (μsec) S-wave	Velocity m/sec P-wave	Velocity m/sec S-wave	Poisson's Ratio ν	Young's Modulus E (MPa)	Wave Amp. P-wave (mV)	Relative Q
213-216	20	2.222	419	745	5569	3134	0.268	71.0	18	6.0
217-220	19	2.209	415	787	5592	2941	0.309	64.5	42.8	6.0
221-224	18	2.188	440	845	5210	2705	0.316	54.8	4.9	7.0
225-228	17	2.174	393	708	5828	3235	0.277	76.2	70	6.0
229-232	16	2.157	390	705	5830	3224	0.280	75.8	60.8	6.0
233-236	15	2.140	394	706	5722	3194	0.274	74.0	38.2	7.0
237-240	14	2.121	381	695	5875	3219	0.286	75.9	112	7.0
241-244	13	2.104	386	725	5749	3054	0.303	69.2	72.8	6.0
245-248	12	2.087	397	730	5536	3007	0.291	66.5	13.0	5.0
249-252	11	2.070	385	754	5671	2883	0.326	62.8	26.2	5.0
253-256	10	2.060	402	737	5393	2939	0.289	63.4	73.0	7.0
257-260	9	2.057	395	737	5485	2934	0.300	63.7	67.6	7.0
261-264	8	2.054	403	705	5363	3070	0.256	67.5	53.0	8.0
265-268	7	2.045	401	740	5367	2905	0.293	62.1	71.2	8.0
269-272	6	2.044	401	726	5394	2962	0.281	64.0	45.2	7.0

Table A.2

Crosshole Seismic Test Results

Transmitter Hole No. C4 Receiver Hole No. C1

Measurement No.	Station No.	Travel Distance (m)	Travel Time (μsec) P-wave	Travel Time (μsec) S-wave	Velocity m/sec P-wave	Velocity m/sec S-wave	Poisson's Ratio ν	Young's Modulus E (MPa)	Wave Amp. P-wave (mV)	Relative Q
273-276	4	2.036	417	804	5128	2651	0.318	52.8	7.4	5.0
277-280	3	2.034	498	960	4255	2201	0.317	36.4	2.30	5.0
281-284	1	2.022	500	1058	4213	1978	0.359	30.3	9.6	5.0
295-298	S5	2.105	642	1169	3384	1858	0.284	25.3	3.8	
291-299	S4	2.071	545	1035	3945	2073	0.309	32.1	5.4	
289-290*	S3	2.044	500	961	4250	2210	0.316	36.6	3.3	
285-289	S2	2.025	509	1041	4141	2017	0.345	31.2	2.7	

* Duplicate Nos. assigned to two records.

Table A.2

Crosshole Seismic Test Results

Transmitter Hole No. C3 Receiver Hole No. C1

Measurement No.	Station No.	Travel Distance (m)	Travel Time (μsec) P-wave	Travel Time (μsec) S-wave	Velocity m/sec P-wave	Velocity m/sec S-wave	Poisson's Ratio ν	Young's Modulus E (MPa)	Wave Amp. P-wave (mV)	Relative Q
26-29	20	2.080	401	711	5459	3081	0.266	68.5	2.9	6.0
30-33	19	2.080	404	736	5417	2971	0.285	64.6	1.46	
34-37	18	2.077	428	797	5091	2747	0.295	55.7	.66	
38-41	17	2.077	377	700	5818	3128	0.297	72.3	7.32	5.0
42-45	16	2.074	386	733	5667	2976	0.310	66.1	3.0	6.0
46-49	15	2.071	412	784	5283	2769	0.311	57.2	1.32	6.0
50-53	14	2.068	406	780	5358	2780	0.316	57.9	.28	6.0
54-57	13	2.065	388	725	5611	2997	0.300	66.5	7.68	6.0
58-61	12	2.062	412	910	5260	2359	0.374	43.6	.92	4.0
62-65	11	2.059	461	1017	4669	2099	0.374	34.5	3.8	6.0
205-208	10	2.057	500	1037	4285	2055	0.357	32.5	1.9	6.0
201-204	9	2.057	505	1024	4241	2084	0.341	33.1	1.6	6.0
197-200	8	2.056	475	1032	4519	2064	0.368	33.2	2.1	6.0
193-196	7	2.056	499	1055	4292	2018	0.358	31.5	2.8	6.0
189-192	6	2.055	450	979	4779	2179	0.369	37.0	5.5	6.0

Table A.2

Crosshole Seismic Test Results

Transmitter Hole No. C3 Receiver Hole No. C1

Measurement No.	Station No.	Travel Distance (m)	Travel Time (μsec) P-wave	Travel Time (μsec) S-wave	Velocity m/sec P-wave	Velocity m/sec S-wave	Poisson's Ratio ν	Young's Modulus E (MPa)	Wave Amp. P-wave (mV)	Relative Q
185-188	5	2.055	476	1051	4507	2025	0.374	32.1	5.6	6.0
181-184	4	2.055	475	927	4516	2306	0.324	40.1	6.2	7.0
177-180	3	2.048	543		3772				1.64	6.0
157-160	S5	2.166	859		2522				.71	
161-164	S4	2.123	572	1010	3846	2180	0.263	34.2	4.36	
165-168	S3	2.088	576		3625				.96	6.0
169-172	S2	2.062	459		4492				2.9	6.0
173-176	S1	2.048	559		3664				3.48	6.0
				Repeat Measurements						
209-212	11	2.059	461	1004	4669	2127	0.369	35.3	3.4	

Table A.2

Crosshole Seismic Test Results

Transmitter Hole No. C3 Receiver Hole No. C2

Measurement No.	Station No.	Travel Distance (m)	Travel Time (μsec) P-wave	Travel Time (μsec) S-wave	Velocity m/sec P-wave	Velocity m/sec S-wave	Poisson's Ratio ν	Young's Modulus E (MPa)	Wave Amp. P-wave (mV)	Relative Q
383-386	20	2.064	391	734	5563	2957	0.303	64.9	2.4	4.0
387-390	19	2.062	398	735	5455	2950	0.293	64.1	.84	4.0
391-394	18	2.059	392	752	5535	2876	0.315	62.0	1.0	4.0
395-398	17	2.056	411	810	5258	2656	0.329	53.4	1.6	3.0
399-402	16	2.051	438	821	4918	2613	0.303	50.7	1.2	6.0
403-406	15	2.048	455	889	4708	2401	0.324	43.5	.54	3.0
407-410	14	2.045	476	905	4485	2353	0.310	41.3	.84	4.0
411-414	13	2.043	449	956	4762	2221	0.361	38.2	1.2	4.0
415-418	12	2.036	433	962	4930	2199	0.376	37.9	4.2	5.0
419-422	11	2.038	442	977	4829	2166	0.374	36.7	2.2	5.0
423-426	10	2.037	508	1042	4174	2025	0.346	31.4	.60	4.0
427-430	9	2.036	451	987	4724	2141	0.371	35.8	.88	4.0
431-434	8	2.036	498	998	4259	2116	0.336	34.1	1.64	4.0
435-438	7	2.035	500	1047	4240	2013	0.355	31.1	1.5	
533-536	5	2.029	547	1062	3850	1978	0.321	29.4	1.6	5.0

Table A.2

Crosshole Seismic Test Results

Transmitter Hole No. C3 Receiver Hole No. C2

Measurement No.	Station No.	Travel Distance (m)	Travel Time (μsec) P-wave	Travel Time (μsec) S-wave	Velocity m/sec P-wave	Velocity m/sec S-wave	Poisson's Ratio ν	Young's Modulus E (MPa)	Wave P-wave (mV)	
537-540	2	2.023	573	1075	3658	1947	0.302	28.1	.6	

Table A.3

Crosshole Seismic Test Results

Transmitter Hole No. 2M9 Receiver Hole No. 2M7

Measurement No.	Station No.	Travel Distance (m)	Travel Time (μsec)		Velocity m/sec		Poisson's Ratio ν	Young's Modulus E (MPa)	Wave Amp.	Relative Q
			P-wave	S-wave	P-wave	S-wave			P-wave (mV)	
565-568	1	2.938	801	1557	3762	1932	0.321	28.1	0.9	8.0
561-564	2	2.949	860	1864	3511	1613	0.366	20.3	0.3	8.0

Table A.3

Crosshole Seismic Test Results

Transmitter Hole No. 2M9 Receiver Hole No. 2M12

Measurement No.	Station No.	Travel Distance (m)	Travel Time (μsec)		Velocity m/sec		Poisson's Ratio ν	Young's Modulus E (MPa)	Wave Amp.	Relative Q
			P-wave	S-wave	P-wave	S-wave			P-wave (mV)	
553-556	1	2.328	635	1275	3785	1879	0.337	26.9	4.4	8.0
557-560	2	2.322	802	1401	2969	1701	0.258	20.7	.72	10.0

Table A.3

Crosshole Seismic Test Results

Transmitter Hole No. 2M12 Receiver Hole No. 2M7

Measurement No.	Station No.	Travel Distance (m)	Travel Time (μsec) P-wave	Travel Time (μsec) S-wave	Velocity m/sec P-wave	Velocity m/sec S-wave	Poisson's Ratio ν	Young's Modulus E (MPa)	Wave Amp. P-wave (mV)	Relative Q
569-572	1	1.654	2098	3490	796	479	0.216	1.6	.9	8.0
573-575	2	1.664	2022	3440	831	489	0.236	1.7	2.1	10.0

Table A.4

Dry Core Velocities

(m/s)

Borehole	Load (MTons)	Vp 1	Vp 2	Vp 3	Vs 1	Vs 2	Vs 3
	C1	5802	5836	5903	3385	3419	3419
		5663	5729	5729	3313	3313	3336
	C2	5614	5709	5709	3321	3321	3343
		5455	5606	5668	3273	3294	3316
		5779	5915	5949	3394	3428	3428
	C3	5542	5698	5730	3314	3324	3358
		5703	5770	5804	3330	3353	3364
		5825	5825	5893	3405	3405	3405
	C4	5679	5843	5843	3392	3392	3392
		5768	5776	5806	3384	3407	3407
Average Value		5653	5776	5806	3351	3366	3377

Table A.4

Saturated Core Velocities

(m/s)

Borehole	Load (Mtons)	Vp 1	Vp 2	Vp 3	Vs 1	Vs 2	Vs 3
	C1	5973	5973	6008	3407	3407	3419
		5832	5832	5832	3302	3313	3324
	C2	5807	5807	5874	3332	3332	3343
		5798	5798	5765	3252	3262	3273
		5985	5985	6020	3417	3440	3452
	C3	5862	5862	5829	3336	3336	3347
		5838	5838	5872	3319	3330	3341
		5928	5928	5928	3382	3382	3382
	C4	5809	5877	5877	3358	3369	3369
		5937	5902	5902	3384	3407	3395
	Average Value	5877	5881	5891	3357	3358	3365

Table A.4

Dry Dynamic Moduli

Borehole	Load (MTons)	Young's Modulus (GPa) 1	2	3	Poisson's Ratio 1	2	3
	C1	81.0	82.5	83.1	.24	.24	.25
		77.5	78.1	78.8	.24	.25	.24
	C2	77.3	78.2	78.9	.23	.24	.24
		74.4	76.4	77.6	.22	.24	.24
		81.2	83.5	83.8	.24	.25	.25
	C3	76.4	78.2	79.6	.22	.24	.24
		78.4	79.7	80.4	.24	.25	.25
		81.9	81.9	82.5	.24	.24	.25
	C4	80.1	81.6	81.6	.22	.25	.25
		80.7	82.1	82.1	.24	.24	.25
Average Value		79.1	80.4	81.0	.23	.24	.24

Table A.4

Saturated Dynamic Moduli

Borehole	Load (MTons)	Young's Modulus (GPa) 1	2	3	Poisson's Ratio 1	2	3
	C1	83.3	83.3	83.9	.26	.26	.26
		78.5	78.9	79.3	.26	.26	.26
	C2	79.3	79.3	80.2	.25	.25	.26
		76.5	76.9	77.0	.27	.27	.26
		83.7	84.5	85.2	.26	.25	.25
	C3	79.9	79.9	80.0	.26	.26	.25
		79.1	79.5	80.2	.26	.26	.26
		82.0	82.0	82.0	.26	.26	.26
	C4	80.2	81.2	81.2	.25	.25	.25
		82.2	82.2	82.3	.26	.25	.25
	Average Value	80.6	80.9	81.2	.26	.26	.26

Table A.4

Rock Quality Factor*

Borehole	Qp Dry	Qp Sat.	Qs Dry	Qs Sat.
C1	36.1	79.6	76.7	95.1
	42.1	70.0	58.1	225.7
C2	45.2	66.4	53.0	83.0
	45.9	140.7	44.7	----
	50.6	54.4	42.1	124.9
C3	61.8	80.0	35.3	105.4
	32.6	56.4	54.3	106.4
	54.6	89.3	49.6	141.6
C4	38.4	65.6	41.8	409.8
	42.2	71.9	45.7	81.5
Average Value	43.4	71.9	50.0	133.5

* Load= 1 metric ton.

Table A.4

Dry Rock Quality Factor

Load (MTons)		Qp 1	Qp 2	Qp 3	Qs 1	Qs 2	Qs 3
Borehole	C1	36.1	44.5	42.2	79.6	60.1	68.5
	C2	50.6	38.6	46.4	54.4	58.1	72.7
	C3	54.6	68.0	64.9	89.3	125.0	168.1
Average Value		46.4	48.9	50.3	72.8	75.9	94.2

Saturated Rock Quality Factor

Load (MTons)		Qp 1	Qp 2	Qp 3	Qs 1	Qs 2	Qs 3
Borehole	C1	56.9	77.1	91.9	109.7	138.3	128.6
	C2	63.5	63.5	54.9	89.5	107.2	89.9
	C3	59.0	63.3	63.9	127.6	150.1	198.3
Average Value		59.7	67.7	68.6	107.8	130.6	131.9

This report was done with support from the Department of Energy. Any conclusions or opinions expressed in this report represent solely those of the author(s) and not necessarily those of The Regents of the University of California, the Lawrence Berkeley Laboratory or the Department of Energy.

Reference to a company or product name does not imply approval or recommendation of the product by the University of California or the U.S. Department of Energy to the exclusion of others that may be suitable.